

<sup>1</sup> **MicroBooNE: Neutron Induced Cosmogenic  $\pi^0$ 's**

<sup>2</sup> **Ryan A.Grosso**

<sup>3</sup> Submitted in partial fulfillment of the  
<sup>4</sup> requirements for the degree  
<sup>5</sup> of Doctor of Philosophy  
<sup>6</sup> in the Graduate School of Arts and Sciences

<sup>7</sup> **UNIVERSITY OF CINCINNATI**

<sup>8</sup> 2017

9

10

©2017

11

Ryan A.Grosso

12

All Rights Reserved

# <sup>13</sup> Table of Contents

<sup>14</sup> List of Figures	ii
<sup>15</sup> List of Tables	iii
<sup>16</sup> 1 Introduction	1
<sup>17</sup> 2 Neutrinos & Neutrino Oscillations	3
2.1 The History the Neutrino . . . . .	3
2.2 Discovery of the Neutrino . . . . .	5
2.3 Neutrinos in the Standard Model . . . . .	8
2.4 Neutrino Interactions . . . . .	9
2.5 Neutrino Mass and Flavor Oscillations . . . . .	12
2.6 Sterile Neutrinos . . . . .	17
<sup>24</sup> 3 The MicroBooNE Detector	18
3.1 Brief History of LAR-TPC's . . . . .	18
3.2 Introduction . . . . .	19
3.3 Time Projection Chamber . . . . .	20
3.4 Light Collection . . . . .	26
3.5 Electronics Readout . . . . .	28
<sup>30</sup> 4 Booster Neutrino Beam	30
4.1 Primary Beam, Target and Horn . . . . .	31
4.2 Neutrino Flux Prediction . . . . .	32

<sup>33</sup>	<b>5 Low Energy Excess and Relevant Cross Sections</b>	<b>35</b>
<sup>34</sup>	5.1 Overview . . . . .	35
<sup>35</sup>	5.2 LSND Excess . . . . .	35
<sup>36</sup>	5.3 Miniboone Excess . . . . .	37
<sup>37</sup>	5.4 Neutral Current $\pi^0$ production . . . . .	38
<sup>38</sup>	5.5 NC-Pi0 in Carbon vs Argon . . . . .	40
<sup>39</sup>	<b>6 Cosmogenic <math>\pi^0</math>'s at MicroBooNE</b>	<b>41</b>
<sup>40</sup>	6.1 Motivation . . . . .	41
<sup>41</sup>	6.2 Traditional Reconstruction . . . . .	43
<sup>42</sup>	6.3 Wire Cell Imaging . . . . .	44
<sup>43</sup>	6.4 Pattern Recognition . . . . .	45
<sup>44</sup>	6.5 Clustering . . . . .	46
<sup>45</sup>	6.6 Track and Shower Selection . . . . .	48
<sup>46</sup>	6.6.1 Track Removal . . . . .	48
<sup>47</sup>	6.6.2 Single $\pi^0$ Reconstruction . . . . .	49
<sup>48</sup>	6.7 Single $\pi^0$ cosmic sample . . . . .	51
<sup>49</sup>	<b>7 Results</b>	<b>56</b>
<sup>50</sup>	7.1 Monte Carlo Simulation . . . . .	56
<sup>51</sup>	7.2 Data . . . . .	59
<sup>52</sup>	7.3 Data-Monte Carlo Comparison . . . . .	59
<sup>53</sup>	<b>8 Conclusions</b>	<b>62</b>
<sup>54</sup>	8.1 Conclusion . . . . .	62
<sup>55</sup>	<b>I Appendices</b>	<b>63</b>

# <sup>56</sup> List of Figures

<sup>57</sup>	2.1 Cowan and Reines first proposed neutrino experiment. . . . .	5
<sup>58</sup>	2.2 The Hadron production cross section around the $Z^0$ resonance from LEP. . . . .	7
<sup>59</sup>	2.3 The Standard Model . . . . .	9
<sup>60</sup>	2.4 Charge and Neutral Current Interactions . . . . .	12
<sup>61</sup>	2.5 This plot shows the appearance and disappearance curves for a 2-flavor ap-	
<sup>62</sup>	proximation as a function of baseline. The values of $\Delta m^2 = 0.0025\text{eV}^2$ and	
<sup>63</sup>	$\sin^2 \theta = 0.14$ are used. . . . .	14
<sup>64</sup>	2.6 Neutrino Mass Hierarchy . . . . .	16
<sup>65</sup>	3.1 Diagram of a Time Projection Chamber . . . . .	19
<sup>66</sup>	3.2 MicroBooNE TPC . . . . .	21
<sup>67</sup>	3.3 MicroBooNE wires measured linear mass density . . . . .	22
<sup>68</sup>	3.4 Tensioning system . . . . .	23
<sup>69</sup>	3.5 Multiple wire planes installed in MicroBooNE . . . . .	24
<sup>70</sup>	3.6 MicroBooNE tension measuring device . . . . .	25
<sup>71</sup>	3.7 MicroBooNE tension map . . . . .	26
<sup>72</sup>	3.8 MicroBooNE tension histogram . . . . .	26
<sup>73</sup>	3.9 PMT optical unit . . . . .	27
<sup>74</sup>	3.10 PMT optical unit . . . . .	28
<sup>75</sup>	3.11 Detector Electronic layout . . . . .	29
<sup>76</sup>	4.1 The Booster Neutrino Campus . . . . .	30
<sup>77</sup>	4.2 BNB Target . . . . .	32

78	4.3	Booster Neutrino Beamline . . . . .	33
79	4.4	BNB Target . . . . .	34
80	5.1	LSND Excess . . . . .	36
81	5.2	MiniBooNE Event topology . . . . .	38
82	5.3	MiniBooNE excess for $\nu$ and $\bar{\nu}$ . . . . .	39
83	5.4	pi0production . . . . .	40
84	6.1	Icarus Cosmic $\pi^0$ . . . . .	43
85	6.2	Wire Cell reconstruction of CORSIKA MC viewed in the BEE viewer . . . . .	46
86	6.3	Shower merging graphic . . . . .	48
87	6.4	pi0Photon . . . . .	50
88	6.5	Reconstructed energy sum and energy product for shower pairs. Both, the reconstructed energy sum and product is less than the true energy deposited.	51
89	6.6	pi0Photon . . . . .	52
90	6.7	pi0Photon . . . . .	53
91	6.8	pi0Photon . . . . .	54
92	6.9	Cosmic $\pi^0$ production by parent process . . . . .	54
93	6.10	pi0Photon . . . . .	55
95	7.1	Enhanced Signal Sample . . . . .	58
96	7.2	Background Sample . . . . .	59
97	7.3	Area normalized Data-Monte Carlo mass distributions . . . . .	60
98	7.4	Direct data Monte Carlo rate comparison . . . . .	61
99	7.5	Direct data Monte Carlo rate comparison . . . . .	61

# <sup>100</sup> List of Tables

<sup>101</sup>	4.1 Beam Production Systematics . . . . .	34
<sup>102</sup>	7.1 Cosiska MC rates . . . . .	57

# <sup>103</sup> Chapter 1

## <sup>104</sup> Introduction

<sup>105</sup> This thesis describes work towards electromagnetic shower reconstruction and steps towards  
<sup>106</sup> a neutral current single  $\pi^0$  cross section measurement motivated from reconstruction tech-  
<sup>107</sup> niques used for neutron induced cosmogenic  $\pi^0$  analysis. This thesis will use data from  
<sup>108</sup> the MicroBooNE Liquid Argon Time Projection Chamber(LArTPC) located at the Fermi  
<sup>109</sup> National Accelerator in Batavia, Il.

<sup>110</sup>

<sup>111</sup> To begin, Chapter 2 will provide some background about the neutrino. We will begin by  
<sup>112</sup> presenting the initial premise for the need of a neutrino-like particle. Then, we will describe  
<sup>113</sup> the theoretical framework used to address how they interact the standard model. Finally we  
<sup>114</sup> will present the phenomenon known as neutrino oscillation and provide some mathematical  
<sup>115</sup> framework to describe it. Chapter 3 begins with a brief history of the LArTPC detector  
<sup>116</sup> technology and its use as a high precision neutrino detector. The chapter continues to  
<sup>117</sup> explain in depth the various subsystems that constitute the MicroBooNE detector. Chapter  
<sup>118</sup> 4 will describe how a neutrino beam is produced and delivered to the MicroBooNE detector.  
<sup>119</sup> It will focus on Fermilab's Booster Neutrino Beam(BNB) which generates a beam of nearly  
<sup>120</sup> pure  $\nu_\mu$  or  $\bar{\nu}_\mu$  around 1GeV in average energy. Chapter 5 will present in detail the claims  
<sup>121</sup> of the electromagnetic  $\nu_e$ -like excess first seen by the LSND experiment and then later  
<sup>122</sup> verified by the MiniBooNE experiment. This chapter will also discuss the neutral current  
<sup>123</sup> cross section, which is the main background in the MiniBooNE excess claim. Chapter  
<sup>124</sup> 6 will introduce MicroBooNE's cosmogenic background and motivate the importance of

understanding the cosmic rate. Here, we will also discuss the motivation to use cosmic  $\pi^0$  events as a means of calibrating the detector energy scale. The cosmic backgrounds are addressed for the oscillation analysis and a future neutral current 1  $\pi^0$  measurement. Next, this chapter will address simulation, reconstruction, and event selection. Chapter 7 will present results from MicroBooNE cosmics data addressing the cosmic  $\pi^0$  rate from neutral induced events.

## <sup>131</sup> Chapter 2

# <sup>132</sup> Neutrinos & Neutrino Oscillations

### <sup>133</sup> 2.1 The History the Neutrino

<sup>134</sup> The story of the neutrino began in Paris on a cloudy winter day in the year 1896. Parisian  
<sup>135</sup> native, Henri Becquerel was experimenting with uranium salts and investigating the newly  
<sup>136</sup> discovered x-ray radiation. [?] He hypothesized that when the salts were energized by sun-  
<sup>137</sup> light they would produce the x-ray radiation. This hypothesis was disproven on the cloudy  
<sup>138</sup> February 27th day when his experiment still detected radiation emitting from the salts in  
<sup>139</sup> the absence of the sun. Becquerel had discovered radioactivity. In the coming years, this  
<sup>140</sup> phenomena was supported by the work of Marie and Pierre Curie in studying the radioac-  
<sup>141</sup> tivity of the element Thorium which lead to their discovery of the elements Polonium and  
<sup>142</sup> Radium. These discoveries would later win Becquerel and the Curie's the 1903 Nobel Prize  
<sup>143</sup> in Physics.

<sup>144</sup>

<sup>145</sup> After radioactivity became an accepted phenomena in the science community, Ernst  
<sup>146</sup> Rutherford discovered that radioactive decay products came in two different forms. He  
<sup>147</sup> labeled them as  $\alpha$ -decay and  $\beta$ -decay. At the time, beta decay was believed to be a two body  
<sup>148</sup> decay where a nucleus  $A$  decays into a lighter nucleus  $A'$  and a  $\beta$ -particle(electron). The  
<sup>149</sup> outgoing energy of the electron from a two body decay is given by equation 2.1. Assuming  
<sup>150</sup> conservation of energy, the value of the outgoing energy should be a discrete.

$$E_e = \frac{m_A^2 + me^2 - m_{A'}^2}{2m_A} \quad (2.1)$$

151 In 1914, James Chadwick had discovered that the energy spectrum of the  $\beta$ -particles  
 152 were continuations as opposed to mono-energetic. While some scientist were willing to  
 153 abandon the requirement of energy conservation, others found this to be an unpalatable  
 154 solution. Unable to attend the 1930 Tubingen physics conference in Germany, Wolfgang  
 155 Pauli wrote a letter to the attendees in which he proposed the first idea of the neutrino.  
 156 An excerpt from his famous December 4th letter is translated from German below [].

157 I have hit upon a desperate remedy to save the “exchange theorem” of statistics  
 158 and the law of conservation of energy. Namely, the possibility that there could  
 159 exist in the nuclei electrically neutral particles, that I wish to call neutrons,  
 160 which have spin 1/2 and obey the exclusion principle and which further differ  
 161 from light quanta in that they do not travel with the velocity of light. The  
 162 mass of the neutrons should be of the same order of magnitude as the electron  
 163 mass and in any event not larger than 0.01 proton masses. The continuous beta  
 164 spectrum would then become understandable by the assumption that in beta  
 165 decay a neutron is emitted in addition to the electron such that the sum of the  
 166 energies of the neutron and the electron is constant...

167 In 1932, Chadwick discovered the neutron we know of today. Unfortunately, this neutron  
 168 was too heavy to be the particle that Pauli had proposed. Expanding on Pauli’s work, Enrico  
 169 Fermi proposed a more complete picture of beta decay and renamed Pauli’s ‘neutron’ to  
 170 what is commonly called a *neutrino*. Fermi’s theory directly coupled the neutron with a  
 171 final state proton, electron, and neutrino. This theory of beta decay,  $n \rightarrow p + e^- + \bar{\nu}_e$   
 172 preserves the law of conservation of energy and would later prove to be a more accurate  
 173 descriptor of the process.

## <sup>174</sup> 2.2 Discovery of the Neutrino

<sup>175</sup> Measuring and detecting neutrinos is a tricky business. In the 1950's, Clyde Cowan and  
<sup>176</sup> Frederick Reines set out to directly measure neutrino interactions for the first time. If a free  
<sup>177</sup> neutrino existed, they hypothesized that they could detect the byproducts from the inverse  
<sup>178</sup> beta decay  $\bar{\nu}_e + p \rightarrow e^+ + n$ . They realized that such a measurement would require a very  
<sup>179</sup> intense neutrino source and a large detector. Their first proposal, which was approved, was  
<sup>180</sup> to detonate a nuclear bomb to supply the large, instantaneous source of neutrinos. A large  
<sup>181</sup> detector filled with liquid scintillator would free fall down a mind shaft recording flashes  
<sup>182</sup> of light from the ionizing positrons before landing on a bed of feathers and foam rubber.  
<sup>183</sup> The original experimental schematic is shown in Figure 2.1. At that time, the theorized  
<sup>184</sup> neutrino cross section was  $10^{-43} \text{ cm}^2/\text{proton}$  while the existing measured limit was still 7  
<sup>185</sup> orders of magnitude short in sensitivity. The bomb experiment would have worked but  
<sup>186</sup> could not provide the level of sensitivity required to confirm detection for neutrino cross  
<sup>187</sup> sections below  $10^{-39} \text{ cm}^2/\text{proton}$ . This was due to background interactions that came in  
<sup>188</sup> time directly from the bomb.

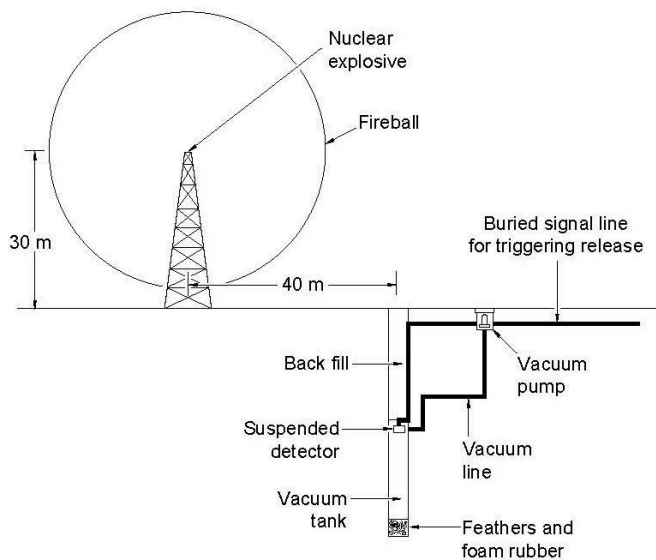
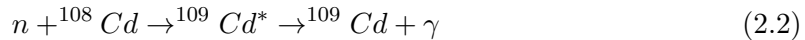


Figure 2.1: Original sketch of Cowan and Reines first proposed neutrino experiment.

Later, Reines realized tagging both the positron and neutron through a double coincidence would drastically reduce the backgrounds. This meant they could use a less intense neutrino source such as a nuclear reactor. They chose the Savannah River Plant near Augusta, Georgia which was estimated to produce neutrino fluxes on the order of  $10^{12} - 10^{13}$  neutrinos/s/cm<sup>2</sup>. The detector was composed of a water target that was doped with CdCl<sub>2</sub>. As stated prior, the signal would rely on a double coincidence flash measured from photomultipiler tubes inside their detector. First, they would detect the positron as it annihilates with an electron via pair production ( $e^+ + e^- \rightarrow \gamma + \gamma$ ). This is identified by two, back-to-back, coincident 0.511 MeV photons. Then, approximately 5μS later, a secondary photon would be detected which was produced from the neutron capture on Cadmium as shown in equation 2.2.



In 1956, only 25 years after Pauli's initial proposal of the neutrino, Cowan and Reines succeeded and provided the first direct experimental evidence of the electron flavor neutrino. In the subsequent years, the existence of two other flavors of neutrinos have been verified. In 1962, Lederman, Schwartz, and Steinberger discovered the  $\nu_\mu$  at Brookhaven Nation Laboratory by measuring neutrinos coming from pion decay. The  $\nu_\mu$  would be distinctly different from that of  $\nu_e$  if the process  $\nu_\mu + n \rightarrow p + e^-$  was forbidden. The results showed that the neutrinos from pion decay were indeed muon-like. Finally in 2000, the DONUT(Direct Observation of NeUtrino Tau) experiment stationed at Fermilab, made the first observed measurement of the  $\nu_\tau$ .

In 1956, C.S. Wu had shown that outgoing electron from beta decay maintained an opposing spin with respect to the spin of the parent nucleus. This turned out to be the first proof of maximal parity violation in weak interactions. Shortly thereafter, the neutrino helicity was first measured at Brookhaven National Labs by Maurice Goldhaber. In nature, neutrinos only have left handed helicity, while anti-neutrinos have right handed helicity. Helicity is frame dependent for particles with mass, which means there can be a reference frame in which the momentum vector can switch but the spin vector will not. For a

216 mass zero particles, this is not possible because the particle would already be traveling at  
217 the speed of light. This assumption is what lead to the believe that neutrinos were massless.

218 The number of active light neutrinos are well constrained by studying the decay of the  
219  $Z^0$  boson at LEP(Large Electron-Positron collider). LEP was an electron-positron collider  
220 ring with a circumference of approximately 27 km that supported four primary experiments  
221 (L3, ALEPH, OPAL and DELPHI). The facility was coined the phrase “Z-Factory” due  
222 to it’s ability to record approximately 1000  $Z^0$  boson decays every hour during optimal  
223 running conditions. The number of active neutrinos,  $N_\nu$  is related to the width of the  $Z^0$   
224 resonance. Using 17 million  $Z^0$ decays, LEP was able to show that  $N_\nu = 2.9840 \pm 0.0082$

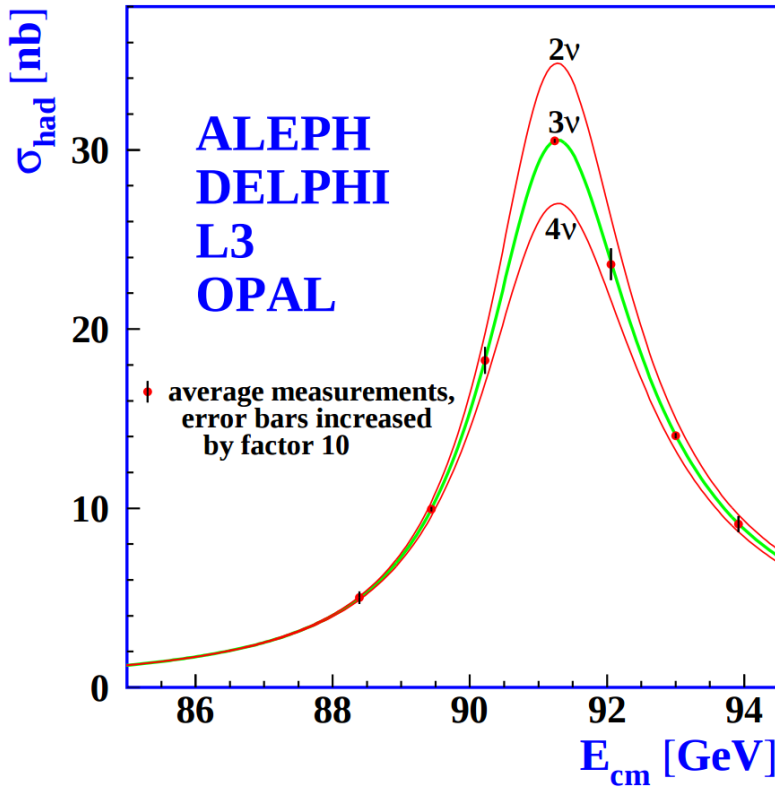


Figure 2.2: The Hadron production cross section around the  $Z^0$  resonance from LEP. The curves for two, three, and four neutrino flavors are shown. The fit shows very compelling evidence of three active flavors of neutrinos.

## 225 2.3 Neutrinos in the Standard Model

226 In the later half of the 20th century, scientists were looking for a way to describe all the  
227 fundamental forces and classify the known particles. The standard model of particle physics  
228 is a phenomenological framework that describes the interaction of fundamental particles be-  
229 tween the strong and electroweak forces. Having stood the test of time, the standard model  
230 accurately predicts most elementary particle interactions, but, does have it's limitations.  
231 The standard model does not account for gravity nor does it account for many new physics  
232 issues such as dark matter or dark energy. Most importantly, as we will see in section 2.5,  
233 it does not provide an accurate description of the neutrino.

234 The standard model consists of two types of particles, bosons and fermions. The funda-  
235 mental bosons consist of two families: gauge bosons, which are typically the force carriers,  
236 and scalar bosons, which refer to spin zero particles or fields. The gluon, photon, and the  
237 weak boson are gauge bosons that mediate the strong, electromagnetic, and weak forces,  
238 respectively. The Higgs boson is a scalar boson that possesses a nonzero vacuum expec-  
239 tation value of  $246\text{GeV}$ . This provides a mechanism for certain particles to gain mass  
240 even though their symmetries would suggest zero mass. The fundamental fermions are also  
241 divided into two families, quarks and leptons each having three generations. The quarks  
242 compose two main categories of particles, baryons and mesons. Baryons consist of an en-  
243 semble of 3 quarks. The most common and stable baryons in the universe are protons( $uud$ )  
244 and neutrons( $udd$ ). Meson consist of an ensemble of quark anti-quark pairs and tend to  
245 have shorter lifetimes than their corresponding baryons. The lightest and most common  
246 mesons are pions( $u\bar{d}, d\bar{u}, u\bar{u}/d\bar{d}$ ) and kaons( $u\bar{s}, s\bar{u}, d\bar{s}/s\bar{d}$ ). The leptons are also divided into  
247 two families with three generations each. The charged leptons, most notably the electron,  
248 interact via the strong and weak nuclear force and combine to form common baryonic mat-  
249 ter. The neutral leptons are the neutrinos and only interact via the weak nuclear force.  
250 More details such as, mass, charge, and spin for various particles are shown in figure 2.3

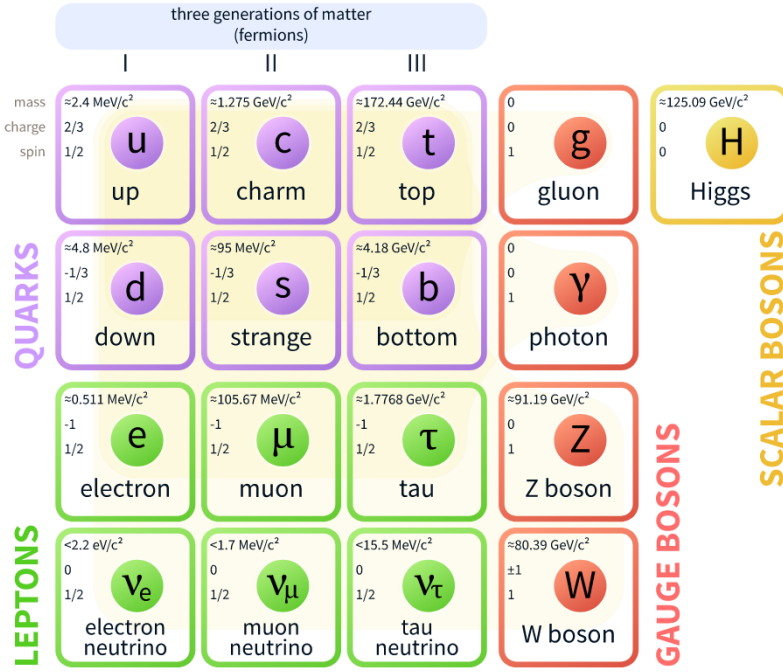


Figure 2.3: The current view of the standard model.

## 251 2.4 Neutrino Interactions

252 Neutrinos interact via the weak force. In the standard model, the weak force is unified  
 253 with the electromagnetic force through an  $SU(2) \otimes U(1)$  symmetry. The structure of the  
 254  $SU(2)$  group symmetry accounts for the chirality of the fermion fields, along with ability to  
 255 produce massive gauge bosons. The  $U(1)$  group symmetry accounts for the massless photon  
 256 propagator needed for electromagnetic interactions. For the quark and fermion families we  
 257 define fermion fields in equations 2.3 and 2.4 , respectively. For formality we will define  
 258 right(left)- handed neutrino(anti-neutrino) fields knowing that they will become irrelevant  
 259 as the theory evolves:

$$\psi_1(x) = \begin{pmatrix} q \\ q' \end{pmatrix}_L, \quad \psi_2 = q_R, \quad \psi_3 = q'_R \quad (2.3)$$

$$\psi_1(x) = \begin{pmatrix} \nu \\ l \end{pmatrix}_L, \quad \psi_2 = \nu_R, \quad \psi_3 = l_R \quad (2.4)$$

260 We begin with the free Lagrangian, defined in equation 2.5, as it is already invariant in  
261 flavor space.

$$\mathcal{L}_{\text{free}} \equiv \bar{\psi}(i\cancel{\partial} - m)\psi = i\bar{\psi}(x)\gamma^\mu\partial_\mu\psi(x) - m\bar{\psi}(x)\psi(x) \quad (2.5)$$

262 To make the Lagrangian invariant under local  $SU(2) \otimes U(1)$ , the fermion derivatives  
263 have to be changed to covariant objects. This produces 4 different gauge parameters, shown  
264 in equations 2.6, which correspond to the 4 different gauge fields required to describe the  
265  $W^\pm$ ,  $Z^0$ , and  $\gamma$ .

$$\begin{aligned} D_\mu\psi_1(x) &\equiv [\partial_\mu - ig\widetilde{W}_\mu(x) - ig'y_1B_\mu(x)]\psi_1(x) \\ D_\mu\psi_2(x) &\equiv [\partial_\mu - ig'y_2B_\mu(x)]\psi_2(x) \\ D_\mu\psi_3(x) &\equiv [\partial_\mu - ig'y_3B_\mu(x)]\psi_3(x) \end{aligned} \quad (2.6)$$

266 Where,  $\sigma^i$  are the Pauli spin matrices and  $B_\mu$  represents a field imposed by an external  
267 source. We find that,

$$\begin{aligned} \widetilde{W}_\mu(x) &\equiv \frac{\sigma_i}{2} \left\{ \partial_\mu W_\nu^i - \partial_\nu^i + g\epsilon^{ijk}W_\mu^jW_\nu^k \right\} \\ B_{\mu\nu} &\equiv \partial_\mu B_\nu - \partial_\nu B_\mu \end{aligned} \quad (2.7)$$

268 The Lagrangian now satisfies  $SU(2) \otimes U(1)$  symmetry between all gauge fields as shown  
269 in equation 2.8. It should be noted that the fermion fields and gauge bosons are required to  
270 be massless. This does not accurately describe the true interaction since 3 of the 4 gauge  
271 bosons are known to have mass, but the theory does allow an interface between neutrino  
272 interactions in the standard model.

$$\mathcal{L} = \sum_{j=0}^3 i\bar{\psi}_j(x)\gamma^\mu D_\mu\psi_j(x) \quad (2.8)$$

273 From equation 2.8, the terms that account for interaction of gauge bosons with the  
274 fermion fields are shown below in equation 2.9

$$\mathcal{L} \rightarrow g\bar{\psi}_1(x)\gamma^\mu\widetilde{W}_\mu\psi_1(x) + g'B_\mu\sum_{j=0}^3 y_j\bar{\psi}_j(x)\gamma^\mu\psi_j(x) \quad (2.9)$$

275 From this, we are then able to construct the Lagrangian for both the charged and neutral  
 276 currents. The charge current Lagrangian is shown in equation 2.10.

$$\mathcal{L}_{CC} = \frac{g}{2\sqrt{2}} \left\{ W_\mu^\dagger [\bar{q}\gamma^\mu(1-\gamma_5)q' + \bar{\nu}\gamma^\mu(1-\gamma_5)\bar{l}] + \dots \right\} \quad (2.10)$$

277 The neutral current term in the Lagrangian contains gauge fields for both the Z boson  
 278 and photon, which can be broken into two terms to account for a non-zero Z boson mass  
 279 while leaving the photon massless through spontaneous symmetry breaking(SSB). This is  
 280 done through an arbitrary rotation, as shown in equation 2.11, where  $\theta_w$  is known as the  
 281 Weinberg or weak mixing angle. This angle is important because it is the angle used to  
 282 rotate through SSB giving the Z boson its mass.

$$\begin{pmatrix} W_\mu^3 \\ B_\mu \end{pmatrix} = \begin{pmatrix} \cos \theta_w & \sin \theta_w \\ -\sin \theta_w & \cos \theta_w \end{pmatrix} \times \begin{pmatrix} Z_\mu \\ A_\mu \end{pmatrix} \quad (2.11)$$

283 It is then possible to write the neutral current Lagrangian that accounts for the inter-  
 284 action of the Z boson as shown in equation 2.13.

$$\mathcal{L}_{NC} = \frac{e}{2\sin(\theta_w)\cos(\theta_w)} Z_\mu \sum_f \bar{f}\gamma^\mu(v_f - \alpha_f\gamma_5)f \quad (2.12)$$

285 where,

$$g\sin(\theta_w) = g'\cos(\theta_w) = e \quad \text{and} \quad \cos(\theta_w) = \frac{M_w}{M_z} \quad (2.13)$$

286 The neutral current coupling constants,  $v_f$ & $\alpha_f$ , differ with respect to the various quark,  
 287 charged and neutral lepton fields. The neutrinos can be described as interactions via the  
 288 charged and neutral currents. The Feynman diagrams, shown in figure 2.4, depict how the  
 289 leptons couple to the quarks via the current mediator.

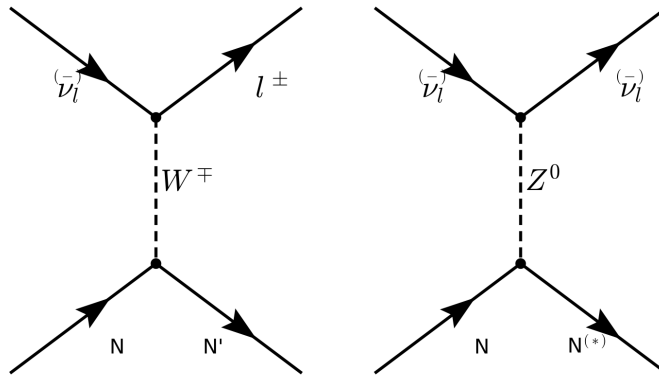


Figure 2.4: The Feynman diagram on the left describes a charged current(CC) neutrino interaction which transforms neutrinos into their corresponding charged leptons. In the CC interaction diagram the  $N \rightarrow N'$  represents a changed nucleon charge. The diagram on the right shows the neutral current(NC) neutrino interaction with preserves the neutrino while it interacts. In the NC interaction diagram the  $N \rightarrow N^*$  represents a same charge nucleon that could be at a higher resonance state.

## 2.5 Neutrino Mass and Flavor Oscillations

Neutrino oscillation is a quantum mechanical phenomenon in which the fraction of neutrino flavor changes while it propagates. This phenomena was first proposed in 1957 by Bruno Pontecorvo and relates the neutrino mass eigenstates with the flavor eigenstates through a rotation. This phenomena is best shown through a two neutrino flavor example, then extended into 3 flavors.

The mixing matrix for a two flavor neutrino case is:

$$\begin{pmatrix} \nu_e \\ \nu_\mu \end{pmatrix} = \begin{pmatrix} \cos \theta & \sin \theta \\ -\sin \theta & \cos \theta \end{pmatrix} \begin{pmatrix} \nu_1 \\ \nu_2 \end{pmatrix} \quad (2.14)$$

In this example, the flavor states are represented as  $\nu_e$  and  $\nu_\mu$  which are expressed as a mixture of mass states  $\nu_1$  and  $\nu_2$ . For ascetic reasons, we chose  $\nu_\mu$  to be part of the example because most man made neutrino beams produce a relative pure sample of  $\nu_\mu$ . The framework for this example is commonly used as an oscillation approximation and can be generalized to satisfy any case of two distinctly different flavor neutrinos.

302 Using the two flavor formalism a pure  $\nu_\mu$  neutrino state can be expressed as equation  
 303 2.15

$$|\nu_\mu(0)\rangle = -\sin \theta |\nu_1(0)\rangle + \cos \theta |\nu_2(0)\rangle \quad (2.15)$$

304 The evolution of the state is governed by solving the time dependent Schroedinger  
 305 equation for the initial muon state:

$$|\nu_\mu(t)\rangle = e^{-i\frac{Et}{\hbar}} |\psi(0)\rangle = -e^{-i\frac{E_1 t}{\hbar}} \sin \theta |\nu_1\rangle + e^{-i\frac{E_2 t}{\hbar}} \cos \theta |\nu_2\rangle \quad (2.16)$$

306 Assuming neutrinos travel near the speed of light, we rewrite equation 2.16 using the  
 307 relativistic approximation, along with setting  $c = \hbar = 1$  and  $p_1 = p_2 = p$ :

$$|\nu_\mu(t)\rangle \simeq -e^{-i(p_1 + \frac{m_1^2}{2p_1})t} \sin \theta |\nu_1\rangle + e^{-i(p_2 + \frac{m_2^2}{2p_2})t} \cos \theta |\nu_2\rangle \quad (2.17)$$

308 with,

$$E = \sqrt{p^2 + m^2} = p \sqrt{1 + \frac{m^2}{p^2}} \approx p + \frac{m^2}{2p} \quad (2.18)$$

309 Next, the mass terms are grouped together and defined as the absolute square difference,  
 310  $\Delta m^2 \equiv |m_2^2 - m_1^2|$ . We find that if the mass are different then the mass eigenstates propagate  
 311 at different frequencies and give rise the oscillatory behavior. The time dependent state can  
 312 now be wrote as:

$$|\nu_\mu(t)\rangle = e^{-i\phi} (-\sin \theta |\nu_1\rangle + e^{+i\frac{\Delta m^2}{2p} t} \cos \theta |\nu_2\rangle) \quad (2.19)$$

with,  $e^{-i\phi} \equiv e^{-i\left(p + \frac{m_1}{2p}\right)t}$

313 To calculate the probability of the initial  $\nu_\mu$  state being measured as a  $\nu_e$  state at some  
 314 later time  $t$ , we need to calculate the absolute value squared of the overlap between the  
 315 states. Utilizing the relationship  $\langle \psi_i | \psi_j \rangle = \delta_{i,j}$ , the overlap between the states is:

$$\langle \nu_e | \nu_\mu(t) \rangle = e^{-i\phi} (-\sin \theta \cos \theta + \sin \theta \cos \theta e^{i\frac{\Delta m^2}{2p} t}) \quad (2.20)$$

<sup>316</sup> The probability reduces to:

$$\begin{aligned}
 P(\nu_\mu \rightarrow \nu_e) &= |\langle \nu_e | \nu_\mu(t) \rangle|^2 \\
 &= e^{i\phi} e^{-i\phi} \sin^2 \theta \cos^2 \theta (-1 + e^{-i\frac{\Delta m^2}{p}t})(-1 + e^{+i\frac{\Delta m^2}{p}t}) \\
 &= \frac{1}{2} \sin^2 2\theta \left( 1 - \cos \left( \frac{\Delta m^2}{2p} t \right) \right)
 \end{aligned} \tag{2.21}$$

<sup>317</sup> Finally, from relativistic assumptions, we set  $p = E_\nu$  as the outgoing neutrino energy  
<sup>318</sup> and  $t = L$  corresponds to the distance traveled.

$$P(\nu_\mu \rightarrow \nu_e) = \sin^2 2\theta \sin^2 \left( \frac{\Delta m^2 L}{4E_\nu} \right) \tag{2.22}$$

<sup>319</sup> From a proper accounting of numerical values of  $c$  and  $\hbar$ , equation 2.26 is more com-  
<sup>320</sup> monly written as:

$$P(\nu_\mu \rightarrow \nu_e) = \sin^2 2\theta \sin^2 \left( 1.27 \frac{\Delta m^2 L}{E_\nu} \right) \tag{2.23}$$

<sup>321</sup> This oscillation behavior is best visualized as a plot of the probability of appearance  
<sup>322</sup> and disappearance as shown Figure 2.5.

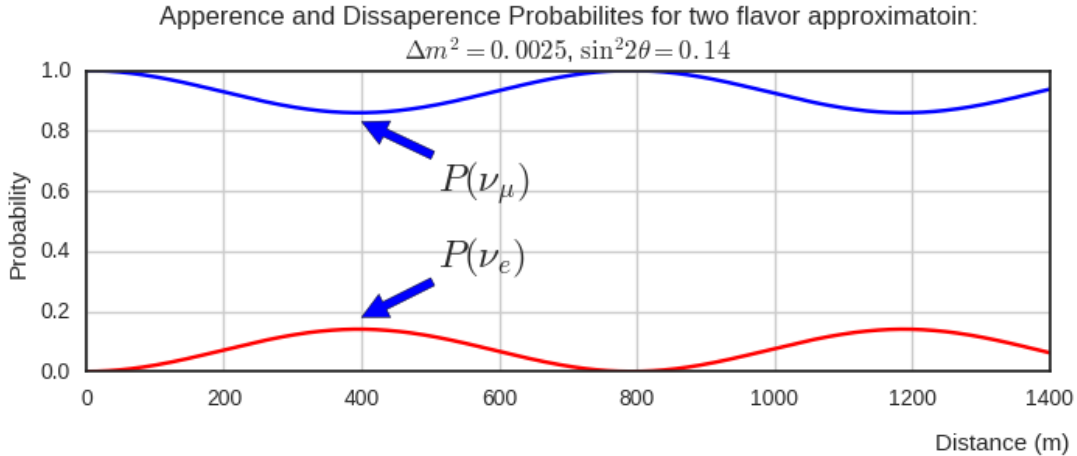


Figure 2.5: This plot shows the appearance and disappearance curves for a 2-flavor approximation as a function of baseline. The values of  $\Delta m^2 = 0.0025 \text{ eV}^2$  and  $\sin^2 \theta = 0.14$  are used.

323 As shown prior from figure 2.2, there are very good constraints on the number of active  
 324 neutrinos. Extending this formalism to a 3 flavor case was done by Pontecorvo-Maki-  
 325 Nakagawa-Sakata (PMNS). The PMNS matrix is a 3 dimensional unitary matrix which  
 326 is parameterized by three mixing angles  $\theta_{12}, \theta_{23}, \theta_{13}$  a complex phase  $\delta$ . The three angle  
 327 correspond to the mixing effect, while  $\delta$  is known as the charge parity(CP) phase. If the  
 328 CP-phase is non-zero, then neutrinos violate charge parity conservation which leads to the  
 329 conclusion that neutrinos and anti-neutrinos interact differently with matter. The value for  
 330  $\delta$  has yet to be observed.

$$U_{PMNS} = \begin{pmatrix} 1 & 0 & 0 \\ 0 & c(\theta_{23}) & s(\theta_{23}) \\ 0 & -s(\theta_{23}) & c(\theta_{23}) \end{pmatrix} \begin{pmatrix} c(\theta_{13}) & 0 & s(\theta_{13})e^{-i\delta} \\ 0 & 1 & 0 \\ -s(\theta_{13})e^{i\delta} & 0 & c(\theta_{13}) \end{pmatrix} \begin{pmatrix} c(\theta_{12}) & s(\theta_{12}) & 0 \\ -s(\theta_{12}) & c(\theta_{12}) & 0 \\ 0 & 0 & 1 \end{pmatrix} \quad (2.24)$$

331 where  $c(\theta_{ij}) \equiv \cos \theta_{ij}$  and  $s(\theta_{ij}) \equiv \sin \theta_{ij}$ . The matrix equation is now put into a more  
 332 compact manor that relates the mixing of the 3 neutrino generations.

$$\begin{pmatrix} \nu_e \\ \nu_\mu \\ \nu_\tau \end{pmatrix} = \begin{pmatrix} U_{e,1} & U_{e,2} & U_{e,3} \\ U_{\mu,1} & U_{\mu,2} & U_{\mu,3} \\ U_{\tau,1} & U_{\tau,2} & U_{\tau,3} \end{pmatrix} \begin{pmatrix} \nu_1 \\ \nu_2 \\ \nu_3 \end{pmatrix} \quad (2.25)$$

333 In it's most general form, the oscillation probability is:

$$P(\nu_\alpha \rightarrow \nu_\beta) = \delta_{\alpha,\beta} - 4 \sum_{j>i} U_{\alpha,i} U_{\beta,i} U_{\alpha,j}^* U_{\beta,j}^* \sin^2 \left( 1.27 \frac{\Delta m_{ij}^2 L}{E_\nu} \right) \quad (2.26)$$

334 From equation 2.26, we see that the oscillation probability is depended on the mass  
 335 difference between states. There is currently no method to directly measure the mass of  
 336 any given neutrino. Therefore, there is an allowed ambiguity in the mass ordering of all  
 337 three neutrino states. This is called the neutrino hierarchy problem. However, we do know  
 338 that the difference between  $m_1$  and  $m_2$  is small relative to  $m_3$ . Using this, we can build  
 339 a picture of the fraction of different flavor eigenstates corresponding to their various mass  
 340 states for both types of hierarchy.

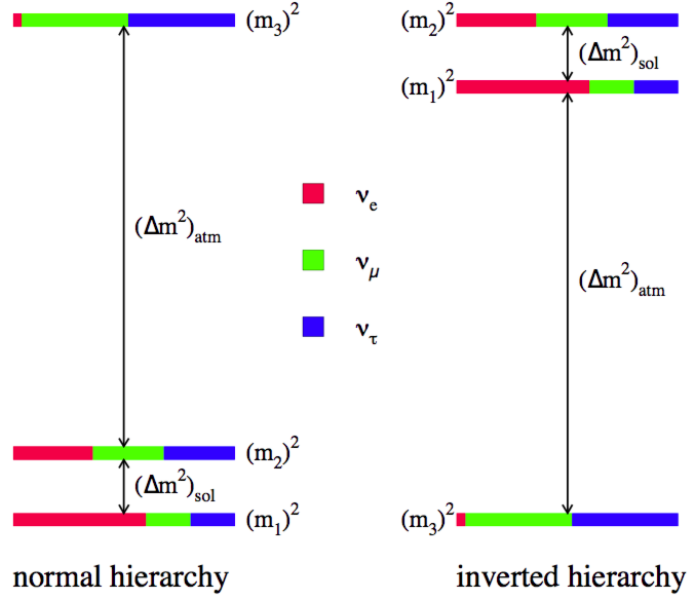


Figure 2.6: The two possible ordering for the 3 active neutrino mass eigenstates.

Many experiments have measures various elements of the PMNS matrix with neutrinos coming from accelerators, reactors, and solar sources. Currently, normal hierarchy ( $m_1 < m_2 < m_3$ ) is favored, therefore we will show (table 2.27) the current Particle Data Group(PDG)[1] best fit values for oscillation parameters with respect to normal hierarchy.

$$\begin{aligned}
 \Delta m_{21}^2 &= 7.37 \times 10^{-5} eV^2 \\
 \Delta m_{32}^2 &= 2.50 \times 10^{-3} eV^2 \\
 \sin(\theta_{12}) &= 0.297 \\
 \sin(\theta_{23}) &= 0.437 \\
 \sin(\theta_{13}) &= 0.0214 \\
 \delta/4 &= 1.35
 \end{aligned} \tag{2.27}$$

345 **2.6 Sterile Neutrinos**

346 It is well accepted, from measurements at LEP[], that there are only 3 neutrinos that couple  
347 through the weak interaction. Mathematically, nothing prohibits a theory that allows for  
348 neutrino mixing with other neutrino states beyond the 3 active states. These states, since  
349 they do not interact weakly, are called 'sterile neutrinos'. Extending the 3 flavor oscillation  
350 model to include any number of sterile neutrinos may be a possibility to address some the  
351 currently unexplained results in the neutrino physics fields. Each additional state requires  
352 an extra dimension to be added to the PMNS matrix. The sterile eigenstates are then  
353 defined as

$$|\nu_{s_i}\rangle = \sum_j^{3+N} U_{s_i,j} |\nu_j\rangle \quad (2.28)$$

354 where N is the number of sterile neutrinos. The necessity for additional sterile neutrinos  
355 was prompted by the LSND experiment and later supported by the MiniBooNE. experiment.  
356 Both experiments are explained in depth in chapter 5. Each experiment found an excess  
357 of electron-like events at low energy. This suggested a  $\Delta m^2$  parameter space observed to  
358 be  $1\text{eV}^2$  larger than expected and strongly contradicted the results of many other results  
359 which had  $\Delta m^2$  around  $\mathcal{O}(10^{-3}\text{eV}^2)$  and  $\mathcal{O}(10^{-5}\text{eV}^2)$ . This precipitated the need for  
360 further exploration of the LSND and MiniBooNE claims with more sophisticated detector  
361 technologies. The MicroBooNE experiment was proposed in 20071 and will be the focal  
362 point for this thesis.

## 363 Chapter 3

# 364 The MicroBooNE Detector

### 365 3.1 Brief History of LAr-TPC's

366 The surprising nature of neutrinos quickly prompted the need for precision measurements  
367 of their interactions. Unfortunately, the low neutrino cross section posed a hurdle to build  
368 a high statistics detector. In 1977, C.Rubbia propose a Liquid Argon Time Projection  
369 Chamber (LArTPC) as large, high precision neutrino detector.<sup>[1]</sup> In 2001, The ICARUS col-  
370 laboration commissioned the T600 detector which was one of the first large scale LArTPC's  
371 to be used as a neutrino detector. <sup>[2]</sup> The T600, which is comprised 760 tons of liquid argon  
372 and commissioned in Pavia, Italy using cosmic rays as a proof of principle. Later the T600  
373 was place underground in Hall B of Laboratori Nazionali del Gran Sasso (LNGS) which is  
374 located 730 km from the source of the CERN neutrino beam.

375 In 2009, the AgroNeut collaboration, commissioned a small LArTPC in a 175 liter  
376 vacuum jacketed cryostat. The ArgoNeut TPC was comprised of 3 wire planes and operated  
377 at a drift field of 500 V/cm. The detector was placed just in front of the MINOS near  
378 detector in the NuMI beam at Fermi National Accelerator Laboratory(FNAL)<sup>[3]</sup>. AgroNeut  
379 collected thousands of neutrino and antineutrino events providing valuable physics data and  
380 detector R&D for future experiments with LArTPC's.

381 The MicroBooNE (the Micro Booster Neutrino Experiment) detector, which will be  
382 discussed in depth throughout this chapter, is the first multi-ton LArTPC to be fully op-  
383 erational in the U.S. The MircoBooNE detector design pioneered many new detector R&D

384 concepts such as: the ability to maintain high LAr purity in an unevaluated vessel, imple-  
 385 mentation of low noise electronic readouts at liquid cryogenic temperatures and advances  
 386 in reconstruction techniques. MicroBooNE also, supports a robust, high statistics physics  
 387 program to address the MiniBooNE Low Energy Excess and various cross section measure-  
 388 ments. MicroBooNE was commissioned and began taking cosmic ray data in the summer of  
 389 2015. In October 2015 it began taking neutrino data. Shortly there after, the first neutrino  
 390 event candidates were identified. []

### 391 3.2 Introduction

392 The MicroBooNE detector utilizes 170 tons of liquid argon to sustain 87 tons of active  
 393 detector mass. It is located at the Liquid Argon Test Facility (LARTF) which is 470  
 394 m downstream of the Booster Neutrino Beam-line(BNB) source at the Fermilab National  
 395 Accelerator Lab (FNAL) in Batavia, Illinois. The detector is the first large scale LArTPC  
 396 to be deployed, commissioned and fully operated in the US.

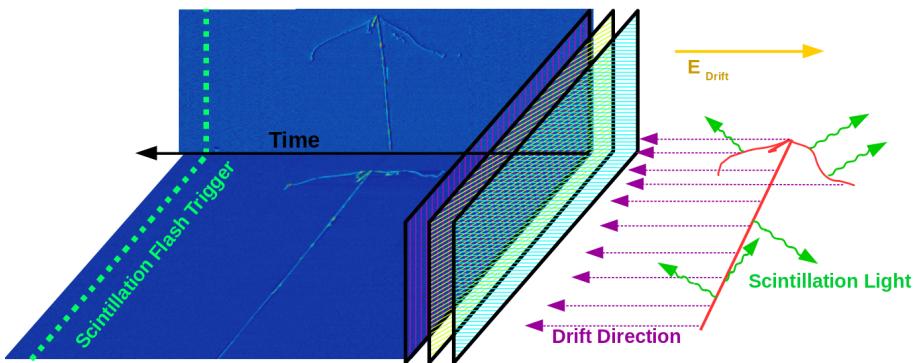


Figure 3.1: This diagram explains how a TPC works. First, charged tracks ionize the argon. The remaining ions produce prompt scintillation light and the corresponding electrons begin to drift towards the wires due to the presence of the electric field. When the drift electrons reach the wire planes a 2D image is produced for each plane. When combining the 2D images from multiple planes along with the scintillation light information a 3D reconstruction is possible.

397 The general principle of a LArTPC involves utilizing two properties of LAr, scintillation

398 light and ionization. Charged particles travel through the argon and produce scintillation  
399 light which is collected by photomultiplier tubes (PMT's). A uniform electric field is applied  
400 over active volume which transports the ionization electrons to a series of wire planes.  
401 Assuming the argon is pure and has minimal electro-negative contaminants, the wire planes  
402 then measure the induced or collected charge signal from the drifting electrons. The planes  
403 are each oriented at a different pitch angles. Each plane then can then produce a two  
404 dimensional image of the event as a function of wire and time. Combining multiple planes  
405 along with the PMT information allows for the object to be fully reconstructed in three  
406 dimensions. A diagram of the TPC concept is show in Figure 3.1. In the following sections  
407 the TPC, light collection system, and electronics are described in detail.

### 408 **3.3 Time Projection Chamber**

409 The TPC is the core of the MicroBooNE detector and forms a rectangular prism with  
410 dimensions  $2.3m \times 2.6m \times 10.4m$  which contains 87t of LAr. The longest dimension, which  
411 in MicroBooNE's coordinate system is refereed to as the z-direction, is oriented on axis  
412 of the BNB. The majority of the TPC materials are composed of 304V stainless steel  
413 and G10. Stainless steel was chosen due to it's low magnetic susceptibility, resistance to  
414 corrosion/oxidation, and ability to maintain it's strength in cryogenic temperatures. G10  
415 was chosen due to it's ability to perform well as an insulator in cryogenic environments.



Figure 3.2: The MicroBooNE TPC is shown here. On the far right is the flat cathode plane. The far left shows the 8,456 anode wires installed. The field cage tubes, which provide the uniform electric field, span the length between the anode and cathode.

416     The TPC field cage, which provides the uniform electric field through the detector  
 417     volume, and was designed to produce field strengths up to 500 v/cm in liquid argon. The  
 418     field cage consists of a total of 64 stainless steel rectangular loops that are supported and  
 419     evenly spaced by a G10 holder. The cathode plane is a series flat stainless steel sheets that  
 420     is opposite the anode sense wires. Figure 3.2 shows the MicroBooNE TPC.

421     Every piece that was used in the MicroBooNE detector was thoroughly cleaned. Many  
 422     pieces were cleaned in an ultrasonic cleansing bath while others were cleaned by hand.  
 423     The detector was constructed in a clean environment that maintained positive pressure to  
 424     mitigate the accumulation of dust. A complete description of the process is summarize in  
 425     a separate technical note. []

426     MicroBooNE has a total of 8,265 sense wires that form 3 unique wire planes, one vertical  
 427     collection plane (Y) and two induction planes ( U,V ) oriented at  $\pm 60$  relative the Y plane.  
 428     The wire planes are separated by 3 mm. The wires in each plane are evenly spaced by 3  
 429     mm pitch on carrier boards. The Y plane consists of 3,456 wires with a total of 108 carrier  
 430     boards that accommodate 32 wires each. Each of the U and V planes consist of 2,400 wires  
 431     with a total of 150 carrier boards that accommodate 16 wires each. The wires themselves  
 432     are made of 304V stainless steel and are  $150 \pm 5\mu\text{m}$  in diameter. A  $2\mu\text{m}$  layer of copper  
 433     is plated over the wires to decrease the resistivity from  $40\Omega/\text{m}$  to  $3\Omega/\text{m}$ . The reduced

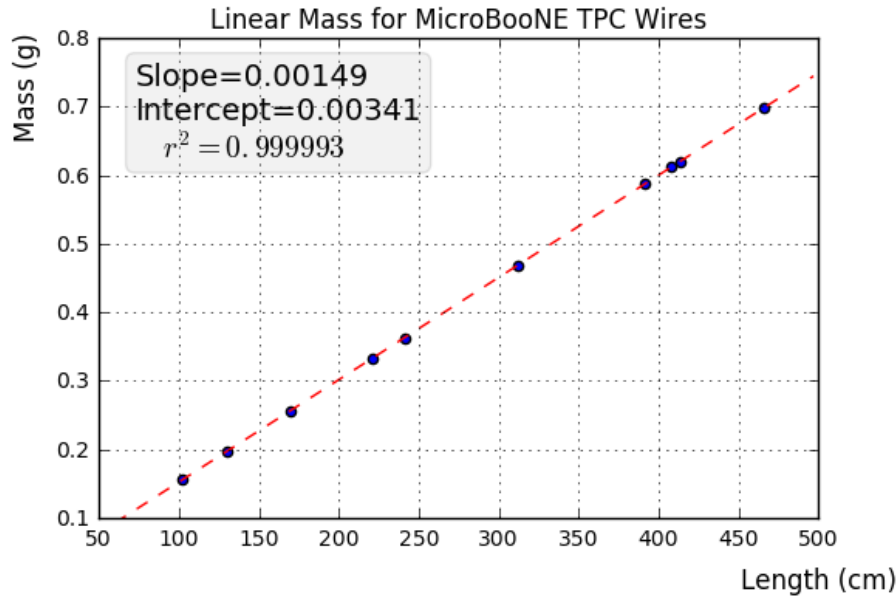


Figure 3.3: This plot is for a small sample used to cross check the linear mass density measured from the wire dealer. The slope from this plot represents the linear mass density and was found to be consistent with the value 0.149g/m

434 resistivity aids in noise reduction at cryogen temperatures. Finally the wire is covered in  
 435 and outer layer 0.1 $\mu$ m of gold to prevent the copper from oxidizing over time. The linear  
 436 mass density of a small sample of wires was measured and is shown in figure 3.3.

437 The wires were designed to installed at a nominal tension of 6.97 N. To account for this,  
 438 the carrier boards were installed onto a series of tensioning bars on the anode frame. These  
 439 tensioning system, as shown in figure 3.4, allowed for fine tune adjustments to be made to  
 440 separate sections of wires.

441 There are a total of 12 tensioning bars, 2 sets of 5 that traverse the entire top and bottom  
 442 length of the anode frame, and 2 spanning the entire height of the upstream and downstream  
 443 sections of the anode frame. Bronze jacking screws were used for final adjustments once  
 444 all the wires were installed. Bronze was chosen since it has a similar thermal expansion  
 445 coefficient to stainless steel and it is a softer metal which helps mitigate the risk of cold  
 446 welding with stainless steel during the tensioning process.

447 In preparation for installing the actual detector wires, an installation team was trained

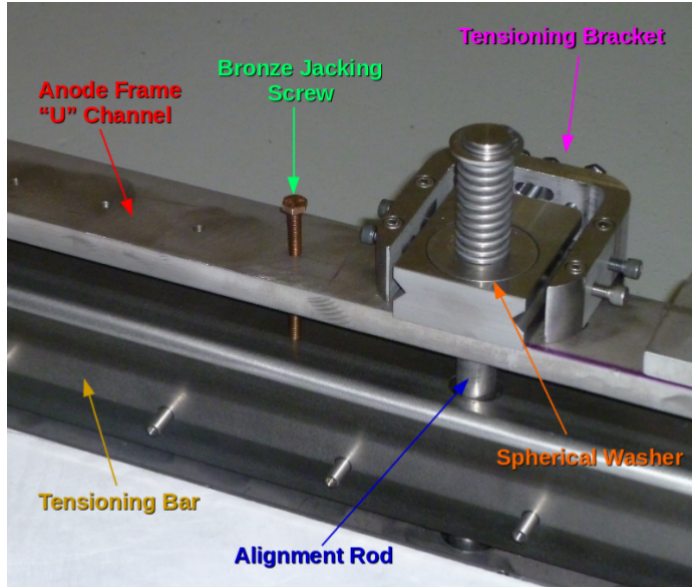


Figure 3.4: The MicroBooNE tension system. Wire carrier boards (not shown here) are mounted on the tensioning bar. The tensioning bar is able to move the wires during the tensioning process. Bronze jacking screws were used for final alignment during the tensioning process

448 on how to properly handle and install them. A 'mock-wire' installation was done to practice  
 449 and identify the risks. After this, the actual wires were installed. The installation took  
 450 approximately one week. The wires were installed serially, first the Y-plane, then the U-  
 451 plane, and then the V-plane. After all the wires were install, a G10 cover board was placed  
 452 over carrier boards to secure and protect the electronics on the board, as shown in figure  
 453 3.5.

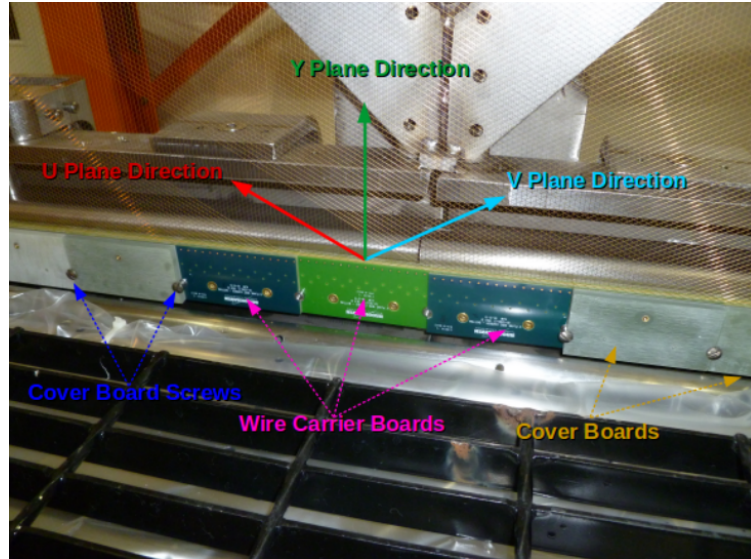


Figure 3.5: The MicroBooNE wires for 3 planes are shown here. The wire carrier boards are serially installed on the tensioning bar. The boards are held in place with a G10 cover plate that is secured with a smooth stainless steel screw.

454 Next, the wires were brought as close to nominal tension as possible. It was decided to  
 455 favor under tensioning wires to minimize the risk of a broken wire during the tensioning  
 456 process. The wire tensioning was done in a systematic way using the bronze jacking screws.

$$f = \frac{1}{2L} \sqrt{\frac{T}{\rho}} \quad (3.1)$$

457 Each wire has a characteristic resonance frequency that is related to its length, tension,  
 458 and linear mass density through equation 3.1. A custom device was made to measure  
 459 the resonant frequency of individual MicroBooNE wires. A laser light was focused on a  
 460 particular wire and the wire gently plucked. A photo-diode mounted in an optical lens then  
 461 measured the intensity of reflected light as the wire vibrated. The signals were then read into  
 462 SpectrumAnalyzer, which is a software package that records frequency. SpectrumAnalyzer  
 463 also allowed the high order frequency harmonics to be seen. The higher frequencies allowed  
 464 for more precise tension measurement as see in Figure 3.6

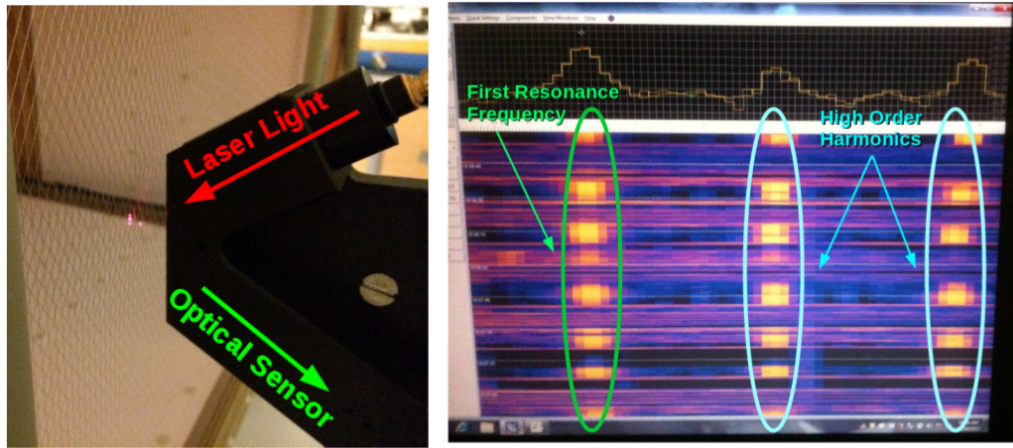


Figure 3.6: Left: Picture of the tension measuring apparatus including a laser and a optical sensor made of a photo-diode and a lens. Right: Example output of the SpectrumAnalyzer showing the first resonance frequency (bright line on the left) and the higher order harmonics (lines in the middle and left).

465 Note that the tension of 2328 out of 2400 U wires, 2308 out of 2400 V wires, and 3410  
 466 out of 3456 Y wires was measured, corresponding to 97.5 % of all wires installed in the  
 467 detector. Only the wires inaccessible to the tension measuring device were not measured.  
 468 The average tension for U,V,Y planes respectively was  $0.589 \pm 0.012$  kg,  $0.664 \pm 0.014$  kg,  
 469  $0.525 \pm 0.009$  kg. The tension for each plane is shown in Figure 3.7 and Figure 3.8.

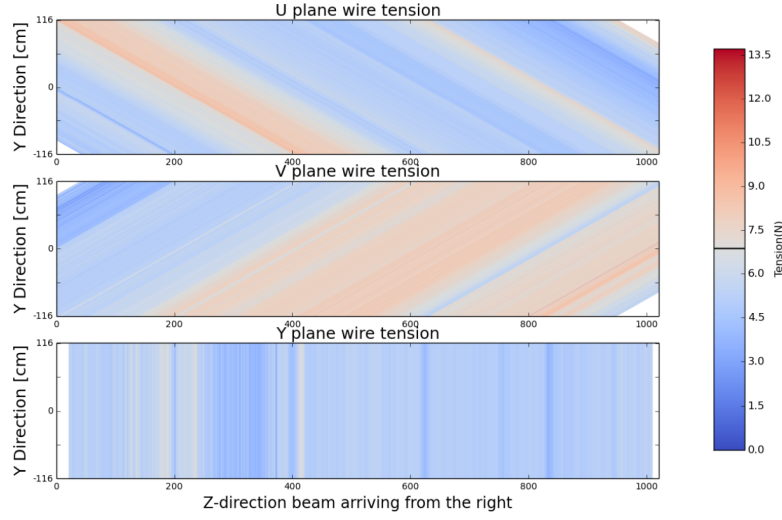


Figure 3.7: This a plane by plane map of the measured wire tensions for MicroBooNE.

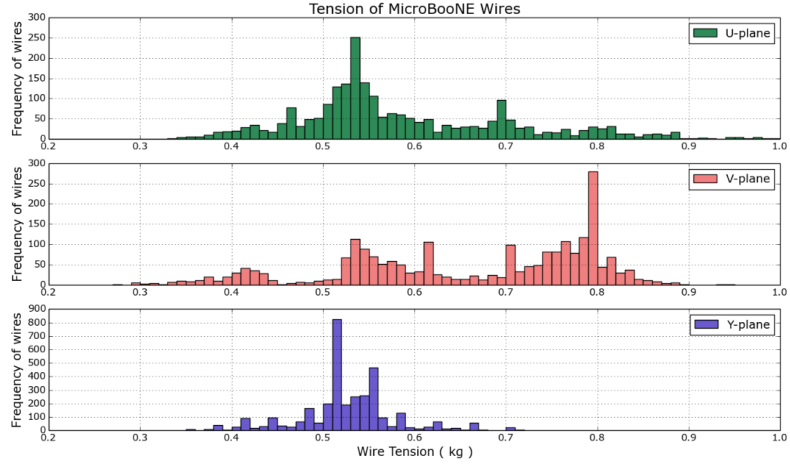


Figure 3.8: This a plane by plane histogram of the measured wire tensions for MicroBooNE.

### 3.4 Light Collection

The TPC can reconstruct 3D objects but there is still an ambiguity in the initial drift position. The light collection system in an LArTPC provides information to address this degeneracy. Scintillation light of liquid argon is 128nm wavelength and is produced through two primary reactions. The first, which accounts for  $\approx 25\%$  of the light yield, is done through a  $\Sigma$  singlet excimer excitation and has a reaction time of  $6 \pm 2$  ns. This type of

476 excimer is formed from an ionized argon atom that combines with another stable argon  
 477 atom. The second, which accounts for the other 75% of light yield, is done through a  $\Sigma$   
 478 triplet excimer excitation and has a reaction time of  $1590 \pm 100 \mu\text{s}$ . The triplet state excimer  
 479 is formed from a stable argon atom, an ionized argon atom, and a free electron.<sup>[1]</sup> Since the  
 480 prompt scintillation light is orders of magnitude faster than drift time from the TPC signal  
 481 this information can be used to address this ambiguity.

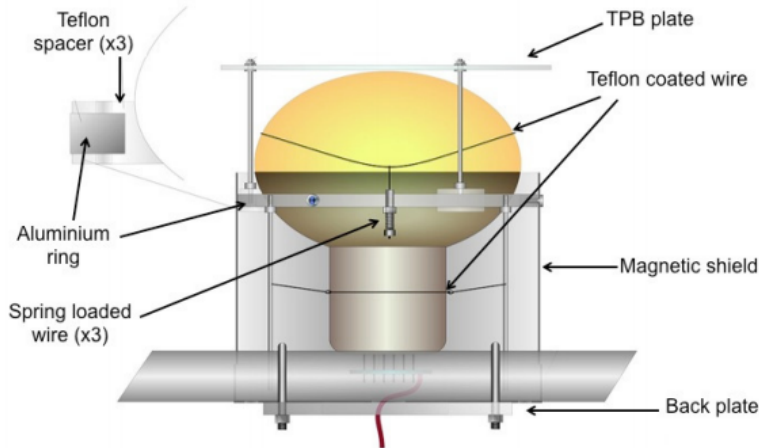


Figure 3.9: Schematic of a PMT optical unit for MicroBooNE.

482 The MicroBooNE light collection system consists of 32 8-inch diameter Hamamatsu  
 483 R5912-02mod cryogenic PMTs. The PMT's are not optimized to detect 128nm vuv light.  
 484 Therefore, an acrylic plate coated with tetraphenyl butadiene(TPB)<sup>[2]</sup> was installed in front  
 485 of the PMT's to act as a wavelength shifter. The TPB plate absorbs the 128nm light and  
 486 re-emits it a peak wavelength of 425nm. Also, it is known that PMT response is reduced  
 487 from certain orientations in the earth magnetic field. To address this a mu-metal shield was  
 488 designed to extend just past the equator of the PMTs. A schematic of a PMT optical unit  
 489 is shown in figure 3.9.

490 The PMT system is mounted on a railing behind the wire planes and spans the entire  
 491 detector length as shown in figure 3.10. This also provides a weak handle on interaction  
 492 position since the scintillation light is fairly localized. Most importantly, since MicroBooNE  
 493 is a surface detector and constantly being bombarded by cosmic rays, the scintillation flash

<sup>494</sup> is used as a method of identifying neutrino interactions coming in time with the beam.



Figure 3.10: PMT optical units installed on support racks inside the MicroBooNE cryostat

### <sup>495</sup> 3.5 Electronics Readout

<sup>496</sup> The TPC and PMT systems produce detector analog signals which need to be digitized,  
<sup>497</sup> transferred out of the detector, and written to disk through data acquisition(DAQ) software.  
<sup>498</sup> Both systems perform a first round of shaping and amplification in the cold LAr and then  
<sup>499</sup> interface with warm electronics for further processing. The DAQ continuously writes to disk  
<sup>500</sup> and creates a buffer which stores data for up to 24 hours. MicroBooNE employs various  
<sup>501</sup> triggers to signify beam and non-beam data blocks and permanently store data from the  
<sup>502</sup> buffer stream. A schematic overview of the TPC and PMT signal processing and readout  
<sup>503</sup> stages is shown in Figure 3.11.

<sup>504</sup> For the TPC, a large portion of the electronics processing for the 8,256 wire signals  
<sup>505</sup> are performed directly in the LAr. To reduce electronics noise, the input distance from  
<sup>506</sup> the wires to the preamplifier is minimized. The sense wires directly interface with CMOS  
<sup>507</sup> analog front end ASICs which operate on cold motherboards. In total MicroBooNE has  
<sup>508</sup> 516 CMOS ASICs. The ASICs generate 50 W of heat load which is a negligible impact on  
<sup>509</sup> the cryogenics system. The motherboards shape and amplify the low noise signal. There

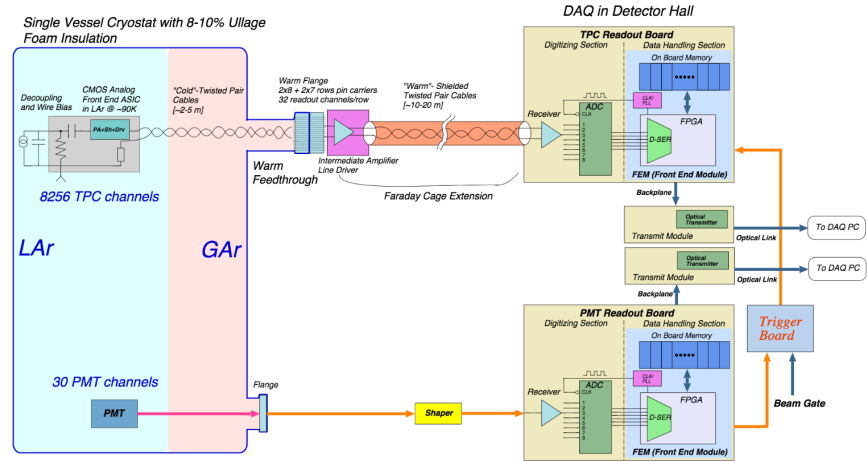


Figure 3.11: MicroBooNE LArTPC and PMT signal processing and readout schematic.

510 are 36 top style motherboards that instrument Y,U and V plane wires and 14 side style  
 511 motherboards that instrument U and V plane wires. The signals are then passed through a  
 512 series of 12 feedthrough ports to warm electronics. The warm signals are then distributed  
 513 over nine readout crates, which digitize the signals.

514 The TPC system read out frame is defined to be 1.6 ms. This number was chosen  
 515 to account for ionization electrons that are generated at the cathode and drift the entire  
 516 distance to the wires in the presence of a 500V/cm E-Field. In MicroBooNE, an event is  
 517 defined as four 1.6 ms readout frames. The additional frames allow for identification of  
 518 cosmic particles that arrive before and after the neutrino interaction.

519 The PMT system is also processed in a similar fashion. The PMT's undergo 60 ns  
 520 shaping to allow for precise measurements of the signal rising edge. The signals are sampled  
 521 at 64MHz but only shaped signals above a threshold are read out and stored for data. The  
 522 PMT signals are split into two different gains. A high gain signal that is 10 times the  
 523 amplitude of the low gain. The signals are then brought to pre-amp/shaper boards and  
 524 digitized and sent to the DAQ.

## 525 Chapter 4

# 526 Booster Neutrino Beam

527 Fermilab is one of the world's leading neutrino facilities and currently produces two neutrino  
 528 beams that span a wide range of neutrino energies. The Booster Neutrino Beam (BNB),  
 529 which will be described in detail throughout this chapter, is a lower energy beam that  
 530 delivers neutrinos to various short baseline experiments. Fermilab also hosts the NuMI  
 531 (Neutrinos at the Main Injector) Beam [] which produces neutrinos over a large range  
 532 between 1GeV/c-30GeV/c and delivers neutrinos to various experiments both on-axis and  
 533 off-axis. The NuMI beam will not be covered in this thesis.

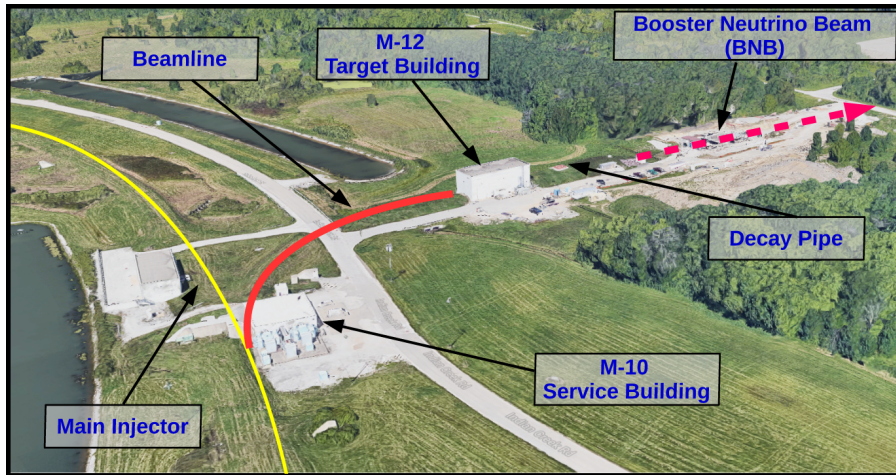


Figure 4.1: This image shows an aerial view of the Booster Neutrino Campus. Protons are extracted before the main injector near the M-10 service building and delivered to the M-12 target hall where the low energy neutrino beam is produced.

534        The Booster neutrino campus is illustrated in figure 4.1. To produce the BNB, pro-  
535        tons are extracted from a transfer line just prior to the main injector and then interact  
536        with a beryllium target. The following sections will describe the beam system, neutrinoos  
537        production process, and flux predictions for the BNB.

## 538        4.1 Primary Beam, Target and Horn

539        The BNB extracts 8.89 GeV/c momentum protons from the Fermilab Booster synchrotron  
540        and delivers them to a beryllium target housed in the M-12 building. The protons from  
541        the booster are grouped in 1.6  $\mu$ s windows called 'beam spills'. One beam spill contains  
542        approximately  $5 \times 10^{12}$  protons. On average the Booster can run no more 5 Hz with no  
543        more than 11 pulses in a row at 15 Hz. In optimal running conditions the Booster can  
544        deliver  $9 \times 10^{16}$  protons on target (P.O.T) per hour.

545        The beam pipe directly leading to the target is approximately 5 feet long and is held  
546        under vacuum to minimize proton interactions not originating from the target. The incom-  
547        ing proton flux is measured by a pair of toroids which are positioned upstream of the target  
548        and provide an error on P.O.T on the order of 2 %.

549        The target consists of 7 cylindrical beryllium slugs that together produce an effective  
550        cylinder of 71.1 cm in length and 0.51 cm in radius. The use of multiple slugs gave the  
551        beryllium more surface area to allow efficient heat transfer from a simple air cooling system  
552        to be sufficient. An exploded view of the BNB target is shown in figure 4.2. As the protons  
553        collide with the beryllium, large amounts of secondary and tertiary mesons, such as  $\pi^\pm, K^\pm$ ,  
554        are produced . These mesons will later decay into neutrinos and other decay particles.

555        The target is positioned inside of a large toroidal electromagnet called a horn. The horn  
556        is made of an aluminum alloy (6061 T6) and is pulsed with 174 kA of current to produces  
557        a  $1/R$  field where R is the distance from the axis of the horn. Since neutrinos are neutral  
558        particles and can not directly be focused by an electric or magnetic force. Instead, the horn  
559        focuses the proper sign parent  $\pi^\pm, K^\pm$  in such a configuration that the neutrino angle from  
560        the parent decay particles are focused in a beam.

561        Directly downstream of the horn/target assembly is a collimator that is used to reduced

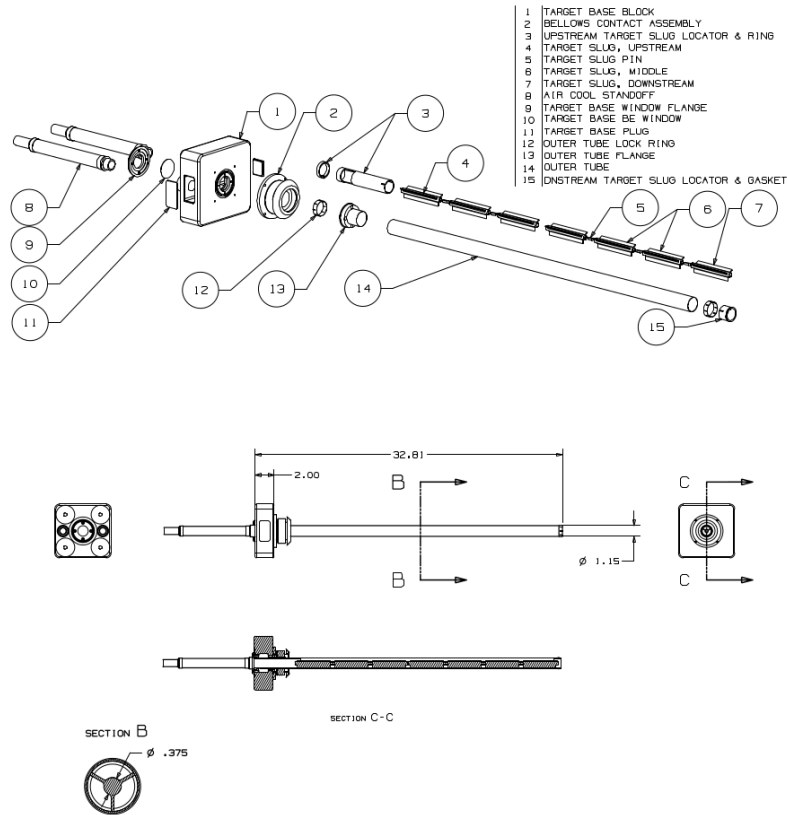


Figure 4.2: An exploded view of the BNB target which shows the 7 Beryllium slugs housed inside the support structure.

background coming from unwanted particles. Particles passing through the collimator enter a 45 m long decay region. In this region, most of the particles decay to produce the neutrino beam. At the end of the decay region there is a beam stop made of steel, concrete. There is also an array of gas proportional counters to detect high energy muons that punch through the beam stop. A diagram of the entire BNB system is shown in figure 4.3. When the horn polarity focuses (negative) positive charged mesons a (anti)neutrino beam is produced.

## 4.2 Neutrino Flux Prediction

The neutrino flux prediction for MicroBooNE uses the same GENIE simulation files used by MiniBooNE. The files are feed into a Geant4 module that simulates the particles as they

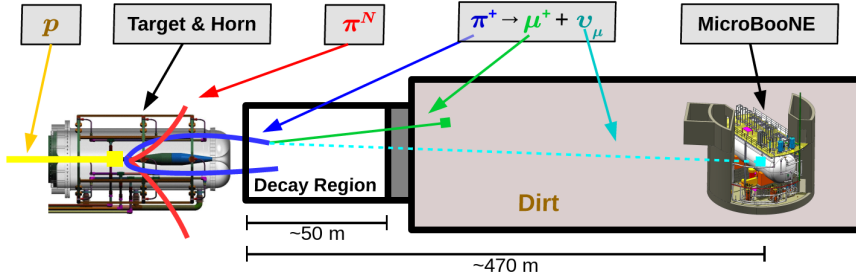


Figure 4.3: This figure shows the Booster Neutrino Beam line at FNAL. The neutrinos are produced in the decay region and then travel towards the MicroBooNE detector located 470 m down stream.

571 travel through the target, horn, and decay region. This produces a MC flux estimate for each  
 572 of the various neutrino types. A systematics study was then performed to provide an error  
 573 estimate for each of the  $\nu_e$ ,  $\bar{\nu}_e$ ,  $\nu_\mu$ , and  $\bar{\nu}_\mu$  flux predictions. To do this, 6 primary systematics  
 574 were varied: the production rates of  $\pi^+$ ,  $\pi^-$ ,  $K^+$ ,  $K^-$ , and  $K_L^0$ , and a group systematic  
 575 comprised of the horn current miscalibration, skin depth, nucleon inelastic, nucleon QE,  
 576 nucleon total cross sections, pion inelastic, pion QE, and pion total cross sections. Beam  
 577 errors for each of systematics are shown in Table 4.1 .The final flux estimate with the error  
 578 uncertainty is shown in Figure 4.4.

	$\nu_\mu$	$\bar{\nu}_\mu$	$\nu_e$	$\bar{\nu}_e$
Delivered P.O.T.	2.00%	2.00%	2.00%	2.00%
$\pi^+$	5.8%	0.46%	4.62%	2.66%
$\pi^-$	0.01%	7.51%	0.28%	3.20%
$K^+$	0.38%	0.13%	5.19%	2.61%
$K^-$	0.01%	0.35%	0.28%	3.92%
$K_l^0$	0.03%	0.27%	2.36%	22.59%
Other	5.78%	6.09%	3.6%	7.61%

Table 4.1: Systematic errors for production of various neutrino types with respect to their, P.O.T. , parent particle, and other variables.

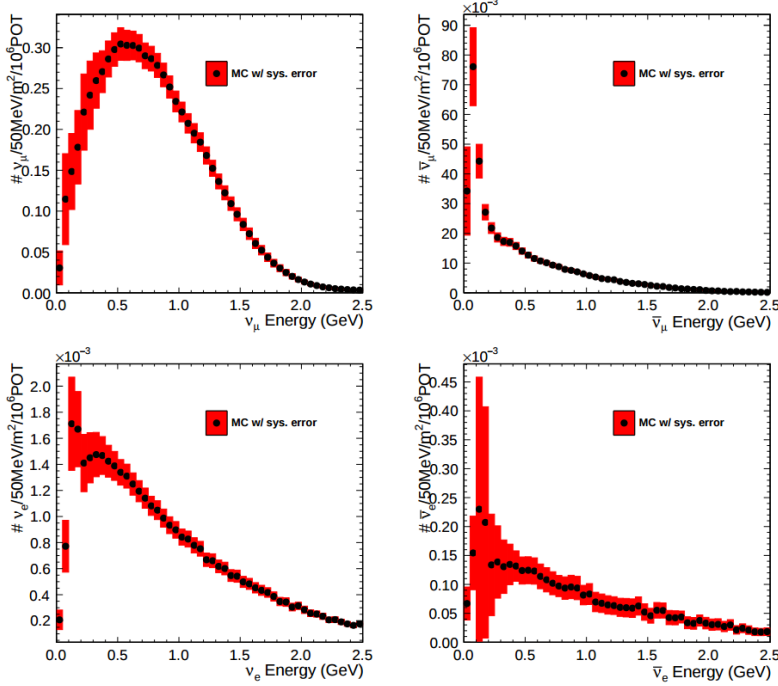


Figure 4.4: Monte Carlo flux predictions for the BNB neutrino spectrum. The red band represents the flux systematic errors. Note the orders of magnitude with the  $\nu_\mu$  spectrum rates.

## 579 Chapter 5

# 580 Low Energy Excess and Relevant 581 Cross Sections

### 582 5.1 Overview

583 This chapter will discuss various facets of what is commonly called the “MiniBooNE Low  
 584 Energy Excess.” First, we will present the anti-neutrino excess observed by LSND and how  
 585 the oscillation results can be interpreted. Then, we will discuss the efforts of MiniBooNE to  
 586 understand the LSND results along with their oscillation results that establish the “Mini-  
 587 BooNE Low Energy Excess.” We will also discuss the neutral current  $1\pi^0$  cross section  
 588 which is the dominant background in the oscillation analysis claims for both MiniBooNE  
 589 and LSND. Finally, we will discuss MicroBooNE’s role towards addressing understanding  
 590 the low energy excess claims of MiniBooNE.

### 591 5.2 LSND Excess

592 The Liquid Scintillator Neutrino Detector (LSND) was a 167 ton neutrino detector stationed  
 593 at Los Alamos National Lab (LANL) designed to study neutrino oscillations. The detector,  
 594 which hosted 1220 PMT’s for event detection, was place 30 m away from the source of a  
 595 low energy ( 40 MeV)  $\bar{\nu}_\mu$  beam. Using the Los Alamos LAMPF beam, 800 MeV protons  
 596 interacted with a water target to produce  $\pi^+$  mesons which decayed into  $\mu^+ + \nu_\mu$ . The  $\mu^+$

597 would then interact with a copper beam stop and decay at rest to produce the low energy  
 598  $\bar{\nu}_\mu$  beam.

599 The detector medium was primarily carbon (mineral oil  $CH_2$ ). LSND could easily  
 600 distinguish between electromagnetic showers (electrons/positrons/photon) or tracks (pi-  
 601 ons/muons/protons) by differences in the Cherenkov cone that was produced. The oscil-  
 602 lation signal interaction was  $p + \bar{\nu}_e \rightarrow n + e^+$ . The primary  $e^+$  is easily visible from the  
 603 Cherenkov light it produced but a neutron will not produce Cherenkov light and therefore  
 604 be invisible to the detector. The organic scintillator b-PDB was dissolved to the mineral  
 605 oil at a concentration of 31 mg/l. The scintillator allowed the 2.2 MeV photon from the  
 606 capture of the neutron on hydrogen to be detected. This allowed LSND a unique signal to  
 607 identify  $\bar{\nu}_e$  interactions. It should be noted that the detector technology could not easily  
 608 discriminate between photons, electrons or positrons induced electromagnetic showers.

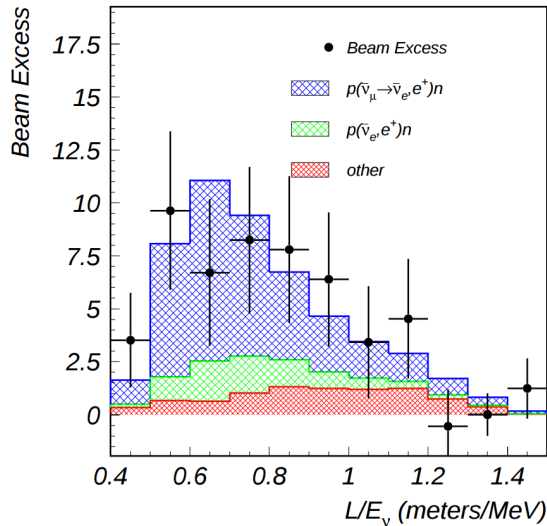


Figure 5.1: This is the LSND neutrino oscillation appearance plot as a function of  $L/E$  and represents the 87 event  $\bar{\nu}_e$  excess claimed by the experiment.

609 In 2001, the collaboration published results for an observed excess of  $87_{\pm 6.0}^{+22.4}$  events  
 610 above the predicted background as shown in figure 5.1. If the excess is interpreted as  
 611 neutrino oscillations from a two neutrino model, the best fit of the excess would suggest a  
 612  $\sin^2(2\theta) = 0.003$  and  $\Delta m^2 = 1.2\text{eV}^2$  which greatly contradicts many other measurements  
 613 for  $\Delta m_{2,3}^2$  or  $\Delta m_{1,3}^2$  [1]. One explanation for the excess suggests the idea of mixing between  
 614 other additional neutrino states. These neutrinos are called ‘sterile’ since they cannot  
 615 directly couple via weak interaction as mentioned prior from the constraints from LEP.

### 616 5.3 Miniboone Excess

617 The Mini Booster Neutrino Experiment(MiniBooNE) was designed to address the claims of  
 618 the LSND  $\bar{\nu}_e$  excess result. The MiniBooNE detector was a mineral oil Cerenkov detector  
 619 designed to be a similar technology to LSND. MiniBooNE, stationed at FNAL in the BNB,  
 620 was positioned 541 m from the neutrino source and was able to receive both  $\nu_\mu$  and  $\bar{\nu}_\mu$   
 621 fluxes. The distance was chosen such that the  $L/E$  parameter were similar to that of the  
 622 LSND experiment.

623 MiniBooNE, which contained 818 tons of mineral oil( $CH_4$ ), was located underneath  
 624 more than 3m of earth overburden to help reduce cosmic rays. The detector supported a 35  
 625 cm thick outer cosmic veto using 240 PMT’s. The veto efficiency was 99.99% for rejecting  
 626 cosmic muons. The inside of the detector was instrumented with 1,280 8-inch PMT’s  
 627 which were used to read out neutrino and comsic data. Cherenkov light from different  
 628 particles produced distinct patterns on various PMT’s inside the spherical detector. A  
 629 cartoon showing various type of signal topologies from the MiniBooNE detector are shown  
 630 in figure 5.2. The detector energy scale was calibrated in situ by fitting various parameters  
 631 from thoroughgoing muons, decay Michele electrons, and  $\pi^0$  decays’s. A clear limitation of  
 632 Cherenkov detectors is the inability to concretely distinguish between photon induced or  
 633 electron induced showers.

634 The primary oscillation analysis for MiniBooNE was done ‘blind’ in an attempt to  
 635 gain confidence from the physics community upon it’s findings. The entire analysis was  
 636 developed on large statistics Monte Carlo simulation and a small sample of test data. In

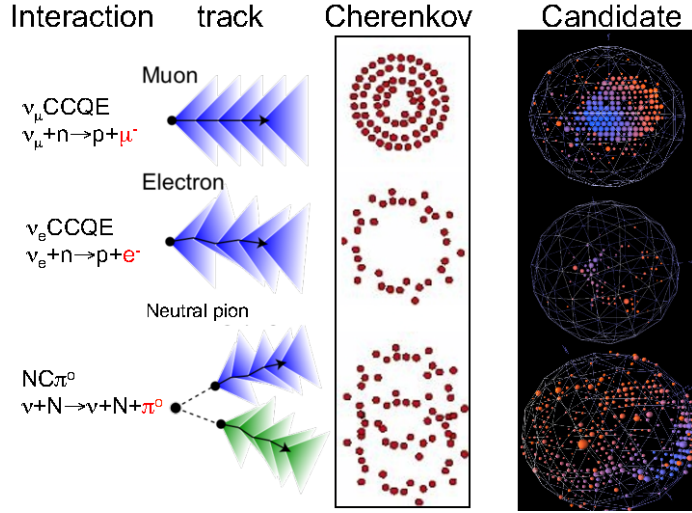


Figure 5.2: This cartoon depicts different particle interactions as observed in Cherenkov detector. The far right shows the interaction types as viewed in MiniBooNE

total, MiniBooNE accumulated  $6.46 \times 10^{20}$ P.O.T. of  $\nu$ -data and  $11.27 \times 10^{20}$ P.O.T. of  $\bar{\nu}$ -data. Fermilab's ability to support both neutrino and anti-neutrino beams allow for MiniBooNE to confirm that an LSND-like excess was independent of neutrino type. The data is in good agreement between signal and background predictions and contradicts the LSND claim up to 98% confidence in both modes above 500 MeV. The excess is most prominent in the region of events below 500 MeV, as seen in figure 5.3. In this region the largest background comes from  $\pi^0$ -misidentification followed by photons coming from radiative Delta decays. MiniBooNE reports a total excess of  $240.0 \pm 62.9$  combine  $(162.0 \pm 47.8\nu, 78.4 \pm 28.5\bar{\nu})$  events in the neutrino energy range  $200 < E_\nu^{QE} < 1250$ MeV. Also, if the excess is interpreted as a two flavor oscillation the inferred parameters are consistent with the LSND result.

#### 5.4 Neutral Current $\pi^0$ production

The leading background from the MiniBooNE oscillation result, as mentioned in chapter 5.3, is  $\pi^0$ -misidentification. Accurately measuring the neutrino induced neutral current single  $\pi^0$  production cross section is therefore crucial in understanding background contributions for an oscillation analysis. Charge current  $\pi^0$  production conveniently has an outgoing

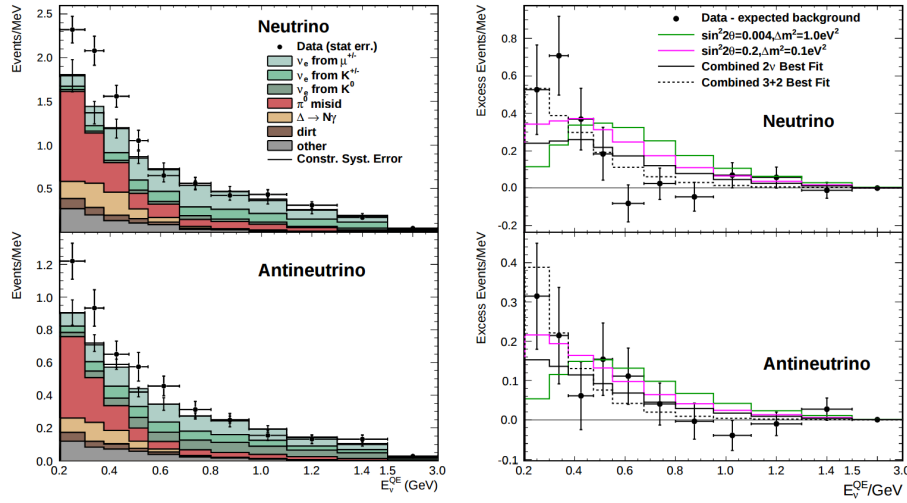


Figure 5.3: The left plots show the stacked histograms for signal and background overlaid with data for both neutrino and anti-neutrino modes. The right plots show the relative excess as a function of neutrino energy and make obvious the energy range that drives the excess.

652 charged muon in the final state and is very easy to identify. On the other hand, neutral  
 653 current  $\pi^0$  production does not guarantee any outgoing charged particles and therefore,  
 654 makes identification much harder. For neutrinos in the BNB, the main production mode  
 655 for neutrino induced neutral current  $\pi^0$  production is via the  $\Delta(1232)$  resonant production.  
 656 Resonant production is when a baryon, such as a proton or neutron, are excited to a higher  
 657 resonance state and then subsequently decays back to the initial state while liberating a  
 658  $\pi^0$ . There are other neutrino induced  $\pi^0$  production modes that MicroBooNE is sensitive to  
 659 such as deep inelastic scattering and coherent production, but have a lower production cross  
 660 section at the given BNB neutrino energy range. A general Feynman diagram can be used to  
 661 describe the main components of neutrino induced neutral current single  $\pi^0$  production in  
 662 argon as seen in Figure 5.4.

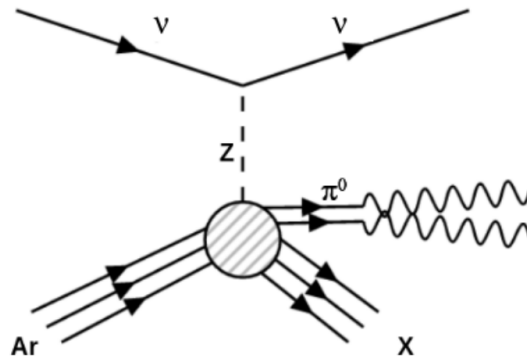


Figure 5.4: Neutrino induced single  $\pi^0$  production on argon. This topology is defined such that 1  $\pi^0$  is produced and the other particles leaving the interaction ( $X$ ) must only consist of nucleons.

## 663 5.5 NC-Pi0 in Carbon vs Argon

664 In 2010, MiniBooNE measured the total neutral current single  $\pi^0$  cross section on carbon  
 665 with what is currently the worlds largest statistics sample of  $\pi^0$ s. The MiniBooNE neutral  
 666 current single  $\pi^0$  signal is defined as a topology that produces one and only 1  $\pi^0$  in the  
 667 final state with no other other charged leptons or mesons originating from the vertex. In  
 668 2015, the first measurement of neutrino induced neutral current  $\pi^0$  production on argon was  
 669 measured by ArgoNeut collaboration at Fermilab while running in the NuMI neutrino beam.  
 670 AgroNeut, being a smaller detector, could not easily contain many of the electromagnetic  
 671 showers from  $\pi^0$  decays. This forced the analysis choose a slightly different final state signal  
 672 definition requiring there to be at least one  $\pi^0$ , no electron or muon, and allowing there  
 673 to be any number of mesons in the final state. This modified signal definition makes any  
 674 comparison to other historical data very complicated.

675 MicroBooNE, which resides in the same neutrino beam line as MiniBooNE, is a prime  
 676 candidate for various studies of neutral current  $\pi^0$  production studies between different  
 677 target materials(C/Ar). Being a larger LArTPC, more  $\pi^0$  decays will be contained allowing  
 678 for high statistics measurements of the cross section along with the general need to measure  
 679 the production rate as input to its own oscillation analysis.

## 680 Chapter 6

# 681 Cosmogenic $\pi^0$ 's at MicroBooNE

682 In this chapter we will talk about some of the challenges and interesting physics cases re-  
683 garding cosmogenics in a surface LArTPC. Many cosmic ray particles penetrate surface  
684 detectors and populate the detector region making it necessary to remove these particles  
685 from reconstruction and address charge contamination in neutrino events. The majority  
686 of this chapter will emphasize cosmogenic track removal, electromagnetic showers and sub-  
687 sequently  $\pi^0$  selection. We will first examine some historical cosmogenic studies from the  
688 Icarus experiment. Then, introduce what MicroBooNE can contribute in terms of under-  
689 standing cosmics. We will address the cosmic simulation that is used, various steps in  
690 reconstruction and pattern recognition used to select  $\pi^0$ 's in a LArTPC. Finally, we will  
691 conclude with how these studies impact future cross section analyses and backgrounds to-  
692 ward the low energy excess analysis.

### 693 6.1 Motivation

694 Cosmogenic particles allow for the separate test of reconstruction tools along with an inde-  
695 pendent way to address the detector energy scale. The high rate of surface cosmics cause  
696 some trouble with disentangling signal neutrino events from cosmic ray removal. Luckily, off  
697 beam surface cosmogenic samples allow for a large statistics dataset to develop and optimize  
698 reconstruction techniques. Cosmogenic muons that traverse the detector provide a handle to  
699 understand detector energy scale along with understanding track reconstruction efficiency.

700 Stopping muons that produce a Michele electron help provide a benchmark for low energy  
 701 showers in the 10's of MeV range. The  $\pi^0$  resonance, with a mass of  $134.9 \text{ MeV}/c^2$ , can  
 702 be used as a standard candle to benchmark overall detector energy scale. The calculated  
 703 the  $\pi^0$  mass, as shown in equation 6.1, depends on a measurement of energy and photon  
 704 opening angle.

$$\mathcal{M} = \sqrt{2E_1E_2(1 - \cos\theta_{12})} \quad (6.1)$$

705 Electromagnetic shower reconstruction for LArTPC's is well known to be a hard task.  
 706 The high resolution of the 2-dimensional projections of EM-showers introduce many chal-  
 707 lenges to develop unbiased and fully automated reconstruction. In 2001, the T600 ICARUS  
 708 detector ?? performed a surface test run in Pavia, Italy. During this 100 day test the detec-  
 709 tor collected over 30,000 cosmic ray events. In 2008, the ICARUS collaboration published  
 710 a study of electromagnetic showers coming from  $\pi^0$  decays in the Pavia dataset. To select  
 711 candidate  $\pi^0$  events, ICARUS hand scanned a total of 7,500 potential events from a PMT  
 712 triggered sample. Their hand scanning requirements included, that at least two well sep-  
 713 arated electromagnetic showers were visible, a valid  $t_0$  time for the vertex, and that there  
 714 was not much charge contamination coming from a nearby cosmic muon. After this, they  
 715 were left with 212 hadronic interactions with at least one candidate neutral which they then  
 716 proceeded to reconstruct. Their final reconstruction consisted of energy scaling to account  
 717 for missing charge in the shower and a minimization against the true  $\pi^0$  mass. An example  
 718 of one of their hand scanned clustering events is shown in Figure 6.1.

719 MicroBooNE, being a surface detector, is in a position to do a similar study with im-  
 720 proved reconstruction techniques. Also, understanding the cosmic production rate for single  
 721  $\pi^0$ 's is valuable to any MicroBooNE analysis that involves EM-showers. The following sec-  
 722 tions will present MicroBooNE's Monte Carlo simulation and state of the art reconstruc-  
 723 tion techniques.

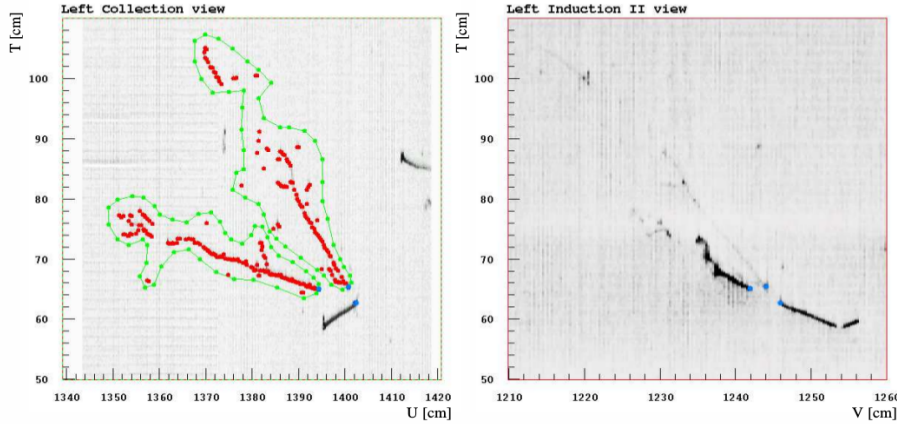


Figure 6.1: A cosmic  $\pi^0$  from the ICARUS Pavia run. The left image shows the hand drawn clustering and positions of the shower conversion point and vertex point. The right image shows the same event on a different wire plane view.

## 6.2 Traditional Reconstruction

The traditional approach for LArTPC reconstruction involves grouping drift charges that are deposited on the wires to form wire-hits. The light collection system also has light-hits which corresponded to collected light of an individual track or shower. A group of PMT's that have light-hits at the same time is called a flash. Hits from each of the wire planes are clustered together with various reconstruction algorithms to form reconstruction objects that relate to individual particles in the detector. There are two primary reconstruction objects: tracks, which are mostly linear and compact clusters that represent muons, protons, and charged pions, and showers which are more fuzzy shaped cluster objects that represent photons and electrons. Next, to reconstruct a 3D object, an algorithm must match the same 2D cluster objects in at least two of the three wire planes. For MicroBooNE, and the general LArTPC community, matching track reconstruction is well advance but shower reconstruction suffers many hurdles. In recent years lots of progress has been made for LArTPC shower reconstruction. Various different techniques such as improved 2D clustering and matching techniques[], sophisticated pattern recognition tools[], and deep learning[] approaches have been explored and each has its various strengths and weaknesses.

<sup>740</sup> **6.3 Wire Cell Imaging**

<sup>741</sup> The traditional approach is not the only way to reconstruct LArTPC data. Instead, wire  
<sup>742</sup> data can be treated with a tomographic approach directly producing a set of 3D space  
<sup>743</sup> points. Although computationally intensive, this approach allows for more information to  
<sup>744</sup> be used in a 3D clustering framework which can directly impact shower reconstruction and  
<sup>745</sup> mitigate degeneracies from the 2D matching method.

<sup>746</sup> The Wire-Cell framework, spearheaded by Brookhaven National Labs (BNL), utilizes  
<sup>747</sup> this approach to create 3D space points from MicroBooNE's TPC data. The approach  
<sup>748</sup> relies on the assumption that the same amount of ionization charge is seen on each plane.  
<sup>749</sup> In MicroBooNE this is done by reconstructing small time slices on each wire planes. Each  
<sup>750</sup> time slice involves solving a charge equation for all possible hits with respect to the matrix of  
<sup>751</sup> hits actually recorded in the time slice. The charge equation is shown in equation 6.2. The  
<sup>752</sup> detector wire signals are represented in matrix W while all potential wire hits are contained  
<sup>753</sup> in H. Nonzero values in the Q matrix will correspond to unique wire-plane intersections of  
<sup>754</sup> charge, near zero values represent ghost hits due to degeneracies in the charge equation.

$$\begin{bmatrix} W_{u_1} \\ \vdots \\ W_{u_n} \\ W_{v_1} \\ \vdots \\ W_{v_n} \\ W_{y_1} \\ \vdots \\ W_{y_n} \end{bmatrix} = \begin{bmatrix} Q_{u_1}^{H_1} & Q_{u_1}^{H_2} & \dots & \dots & \dots & Q_{u_1}^{H_{m-1}} & Q_{u_1}^{H_m} \\ \vdots & \vdots & \ddots & \ddots & \ddots & \vdots & \vdots \\ Q_{u_n}^{H_1} & Q_{u_n}^{H_2} & \dots & \dots & \dots & Q_{u_n}^{H_{m-1}} & Q_{u_n}^{H_m} \\ Q_{v_1}^{H_1} & Q_{v_1}^{H_2} & \dots & \dots & \dots & Q_{v_1}^{H_{m-1}} & Q_{v_1}^{H_m} \\ \vdots & \vdots & \ddots & \ddots & \ddots & \vdots & \vdots \\ Q_{v_n}^{H_1} & Q_{v_n}^{H_2} & \dots & \dots & \dots & Q_{v_n}^{H_{m-1}} & Q_{v_n}^{H_m} \\ Q_{y_1}^{H_1} & Q_{y_1}^{H_2} & \dots & \dots & \dots & Q_{y_1}^{H_{m-1}} & Q_{y_1}^{H_m} \\ \vdots & \vdots & \ddots & \ddots & \ddots & \vdots & \vdots \\ Q_{y_n}^{H_1} & Q_{y_n}^{H_2} & \dots & \dots & \dots & Q_{y_n}^{H_{m-1}} & Q_{y_n}^{H_m} \end{bmatrix} \begin{bmatrix} H_1 \\ H_2 \\ \vdots \\ H_{m-1} \\ H_m \end{bmatrix} \quad (6.2)$$

755        Then, each ‘slice’ is stacked to it’s corresponding x position. This produces a set of 3D  
756        space points that can used in patter recognition algorithms to identify different particles  
757        in the data. All reconstruction is done with accounting for known detector dead regions.  
758        The current state of MicroBooNE’s signal and noise processing and imaging that requires  
759        a minimum of 2 wire planes to be matched from the charge equation.

760        **6.4 Pattern Recognition**

761        Various pattern recognition tools are needed to address MircoBooNE’s TPC data but for  
762        this analysis they can be generalized into two efforts, cosmic track removal and EM-shower  
763        clustering. Both approaches require different techniques. First, we will focus on optimizing  
764        track removal. This involves identifying tracks that are through-going, and contained. Once  
765        all the charge associated with tracks are removed, the remaining charge is clustering into  
766        candidate EM-shower objects. Finally, correlated shower pairs are identified and selected  
767        as candidate  $\pi^0$ events.

768        A image of a typical MicroBooNE cosmic event reconstructed with 3D wire cell space  
769        points are shown in Figure 6.2 using the BEE viewer []. A detailed list of reconstruction  
770        and selection parameters are listed in appendix ??

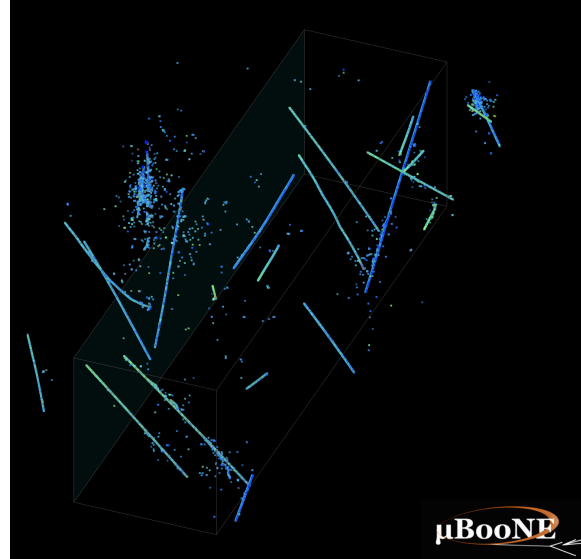
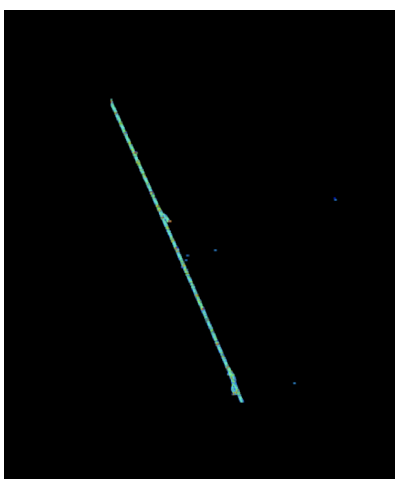


Figure 6.2: This is a typical cosmic event in the MicroBooNE detector. The data used to generate this event is CORSIKA Monte Carlo.

## 6.5 Clustering

The wire cell data produces a set of 3D space points as mentioned in section 6.3. Only space points that are in the fiducial volume are clustered and considered in the reconstruction process. First a charge threshold cut of 0.5 MeV is applied to all the remaining space points. This is to remove very low charge ghost points and reduce the overall number of points to cluster. The main goal of this step is to identify the large scale structure of the cosmic tracks in the data. Additionally, with a smaller number of space points the computational time for reconstruction is reduced.

The first stage of clustering uses BIRCH (balanced iterative reducing and clustering using hierarchies). The hyper parameters were tuned such that cosmic tracks are removed with minimal impact to showers involved from  $\pi^0$ . Birch clustering was chosen because it scales well with large number of points, efficiently maintains large number of clusters in datasets and also handles outliers removal well. This clustering technique leverages on the inherent structure of charged particle tracks having a well define 3-dimensional trajectory. Particles such as protons, muons, and charged pions are continuously ionizing meaning that there should be not be gaps in the detected charge. This feature is much different than



(a) This figure shows an image of muon track as viewed from the BEE-WireCell image viewer.



(b) This figure shows an image of  $\pi^0 \rightarrow \gamma\gamma$  decay as viewed from the BEE-WireCell image viewer.

787 EM-showers which have lots of gaps between detected charge. An example of this is shown  
788 in figure ??

789 The next stage of the track and shower clustering process is to merge together proto-  
790 clusters that did not get fully grouped together in the BIRCH clustering step. The second  
791 pass clustering is geared toward larger object clustering. To address this, a 3D convex hull  
792 is constructed around every cluster. Next, the euclidean distance between all the vertex  
793 points are calculated. If the minimum merging distance is small, as it is for many charge  
794 particle tracks, the clusters get merged together well. Clusters from showers, as they tend  
795 to be very spread out, still need further merging.

796 The final stage of clustering is shower clustering. This requires there to be a distinction  
797 between a cluster object that is shower-like or track-like. To do this, parameters that  
798 describe various aspects of a cluster are calculated. The most important features from  
799 the cluster parameters are cluster length and spread of the first principle component. More  
800 details about track and shower selection are described later in section 6.6.

801 Once defined as a shower cluster, a 3D charge weighted axis is fit to the cluster's set  
802 of space points. First, a distance of closest approach (DOCA) for each cluster axis pair  
803 is calculated and a proto-vertex is calculated at the midpoint of the DOCA line. Next, a

unique conversion point is calculate for each shower pair to identify the start point of the shower. This can also be thought of as a proxy for the photons conversion point. Using the proto-vertex point and two conversion points an opening angle is calculated. A pair of clusters that have a DOCA that is less than 5 cm, an angle between 15 and 165 degrees, and both of the conversion lengths are less than 20 cm are merged together. The merging is done for all shower cluster pairs as a final stage of the merging process.

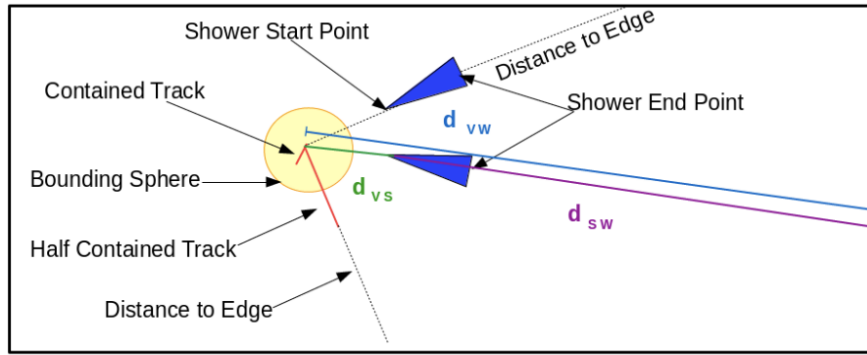


Figure 6.3: This graphic illustrates all the data objects and relevant parameters. The shower objects are shown in blue, track objects shown in red, and a bounding sphere, used to associate tracks with the vertex, is shown in yellow.

## 6.6 Track and Shower Selection

### 6.6.1 Track Removal

For this analysis track removal is handled in a unique manner. The primary goal is to identify showers coming from a  $\pi^0$ . Therefore, all cuts and optimizations will be tested against shower objects. Being that we simply are trying to identify charged tracks and not particle type, the charge information is not used. The general approach for track removal depends heavily on geometric properties such as length and linearity of the cluster.

817    **6.6.2 Single  $\pi^0$  Reconstruction**

818    The vast majority (98.8%) of  $\pi^0$ 's decay into two photons. The relationship for the particle  
819    mass, which was defined in eq 6.1, shows the importance of properly accounting for the  
820    energy and angle between the decay photons. To understand a baseline for reconstruc-  
821    tion efficiency we have generated a sample of 10,000 single particle  $\pi^0$  events isotropically  
822    throughout the detector volume with initial momenta spanning from 0 to 2 GeV.

823    First we will investigate energy deposited in detector from the decay. An plot of the true  
824    kinematic energy of photons from the decay particle is shown in Figure 6.4. It is important  
825    to note that both photons need to be reconstructed to form a mass. This means that we  
826    are driven to optimize the reconstruction to be robust around showers in the range of many  
827    10's of MeV in deposited energy. Photons that convert near the fiducial edge of the detector  
828    can escape and deposit only a small amount of energy in the detector. This poses problems  
829    for capturing the total amount of energy of the shower and drives the need for a fiducial  
830    cut around the edges.

831    To understand the reconstruction accuracy for the energy we are most interested in two  
832    metrics. The first is the total collected energy deposited by the two showers. This informs  
833    us that we are accounting for most of the energy deposited and handling the fiducial cuts  
834    well. The second is the product of the two shower energies. This directly impacts the  
835    reconstructed mass resolution and informs us that we are clustering energy between the  
836    two showers properly. In figure 6.5 both metrics are plotted for reconstruction against true.  
837    Points along the diagonal would represent accurate model predictions. As we will see later  
838    in this chapter, the energy product drives the width of the mass resolution.

839    Next we will investigate the effects of the opening angle between the two photons.  
840    The minimum opening angle of the photons is constrained by the momentum boost as  
841    the particle decays as shown in equation 6.3. The angular resolution is a very challenging  
842    problem in LArTPC's using the traditional 2D projection approach. Fortunately, direct  
843    3D reconstruction improves the angular resolution and allows for a better measurement of  
844    shower direction.

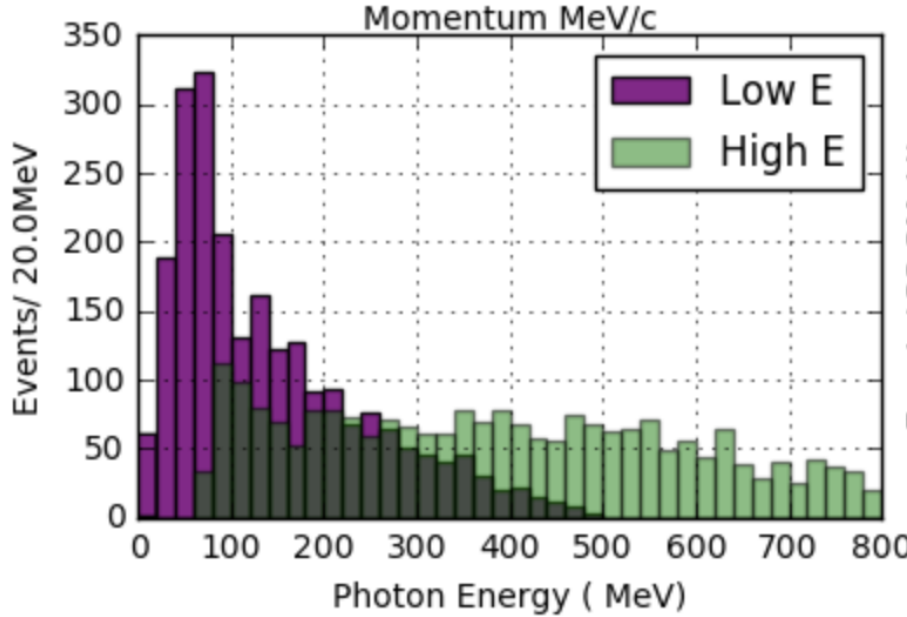
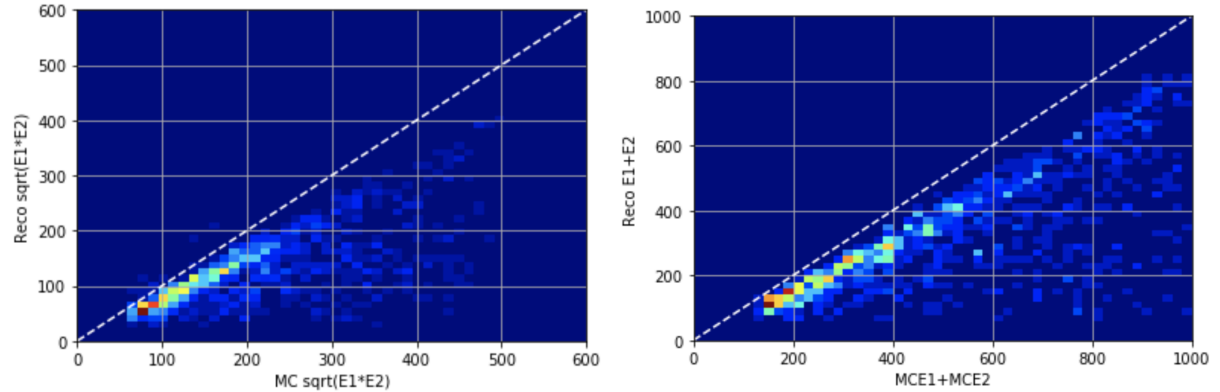


Figure 6.4: This figure shows the photon distribution for  $\pi^0$  decays from a single particle sample of between 0-2 GeV. The higher energy photon is shown above in green along with the corresponding lower energy photon shown in magenta.

$$\sin \frac{1}{2}\theta_{min} = \frac{M}{E_{\pi^0}} \quad (6.3)$$

845 A plot of the reconstructed vs true opening angle is shown in Figure 6.6. The  $1 - \cos\theta$   
846 term from equation 6.1 is sensitive to tails of the mass distribution.

847 Next, we apply a final set of selection cuts. First, we require that the distance of closest  
848 approach between the two shower axis is less than 5 cm. This is to help ensure that the  
849 photons are originating from a common origin. Next, the photon conversion distance can  
850 not be longer than 70 cm. This is done to help identify showers that are correlated from  
851 the same decay. Finally we only accept showers that are above 50 MeV in reconstructed  
852 energy. Figure 6.7 shows the effect of various parameters as applied to the reconstruction.  
853 We find that the deficit in mass peak is mainly due to the energy reconstruction. This is  
854 due to the missing energy during clustering. For this analysis there is also an additional  
855 component of energy missing since we will not be using the initial  $t_0$ -tag. The  $t_0$ -tag is



(a) Scatter plot of reconstructed energy sum vs true energy sum  
(b) Scatter plot of reconstructed energy product vs true energy product

Figure 6.5: Reconstructed energy sum and energy product for shower pairs. Both, the reconstructed energy sum and product is less than the true energy deposited.

856 used to identify how far the electrons had to drift to reach the wire plane. Without using  
857  $t_0$ , there is no effective way to correct back for electron drift effects. Thankfully, this effect  
858 is can be captured in understanding the distribution of reconstructed mass peak in the  
859 Monte Carlo.

860 Finally, we address the over all efficiency for reconstruction. The average reconstruction  
861 efficiency between 0 and 1 GeV/c is 40.1%. The reconstruction efficiency is shown in Figure  
862 6.8. As can be seen there, the efficiency drops at low and high energies. At low momentum  
863 the  $\pi^0$ 's are produced nearly at rest with both showers having similar energies. Most  
864 importantly the showers are produced nearly back to back. Without having a well defined  
865 vertex, sometime the reconstruction will identify the angle as being close to zero. Being  
866 that there is a minimum opening angle cut some of the events are lost from this effect. At  
867 high momentum, many of the showers are boosted to small opening angle which we see a  
868 similar effect in the loss of efficiency.

## 869 6.7 Single $\pi^0$ cosmic sample

870 The MicroBooNE cosmics Monte Carlo is generated by CORSIKA(COsmic Ray Simula-  
871 tion for KAscade) v-7.4003[?] CORSIKA simulates particles coming from a wide range of

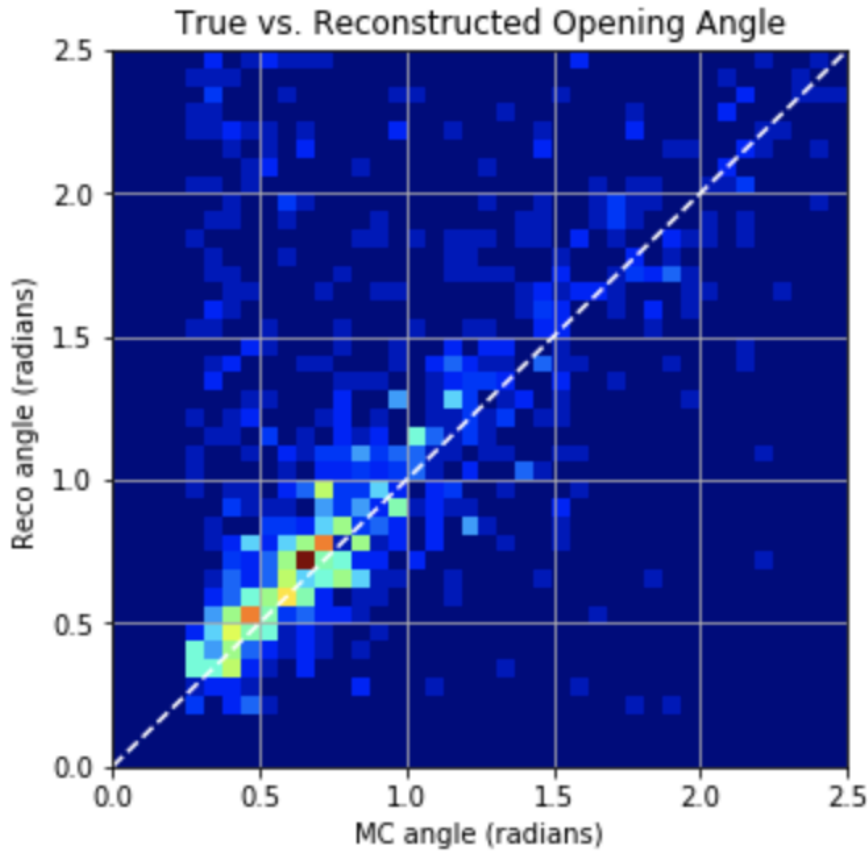


Figure 6.6: This scatter plot shows the reconstructed opening angle vs. true opening angle. We see that the reconstruction does very well with reconstructing this quantity due to the use of wire-cell's 3D approach. When the reconstruction performs badly it tends to identify small opening angles as large ones since we are not using any vertex information.

872 interactions initiated by cosmic ray particles in the upper atmosphere. The simulation is  
 873 robust and accounts for various input parameters such as, longitude and latitude, elevation,  
 874 and the earths magnetic field. The particles are simulated over a large region above the  
 875 detector complex but only particles that travel through the detector cryostat volume are  
 876 kept. The passage of these particles simulated by the GEANT4 package. Cosmic rays that  
 877 do not travel through the cryostat have a low likelihood of producing secondary or tertiary  
 878 particles that enter the detector TPC volume [?]

879 In one MicroBooNE drift window (2.3ms) there are on average 6 cosmic muons. The

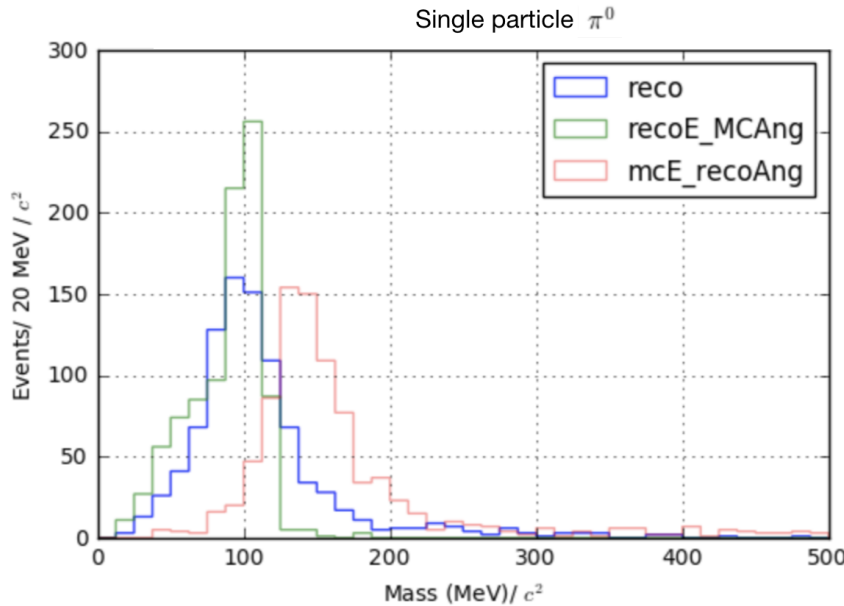


Figure 6.7: The reconstructed mass distribution is shown to highlight effects from reconstruction. First, in blue, the full reconstructed mass is shown. Second, in green, the reconstructed mass is calculated using the true angle. Third, in red, the reconstructed mass is calculated using the true energy.

880 muons do not directly contribute to many EM-showers but sometimes pass through an EM-  
 881 shower from another particle. For MicroBooNE, the vast majority of muons are through  
 882 going and do not lead directly to any method of  $\pi^0$  production.

883 Various other particles such as, protons, neutrons, and charged pions enter the TPC  
 884 volume and may produce  $\pi^0$ 's. A distribution of  $\pi^0$  production process is shown in Figure  
 885 6.9. Nearly half of the  $\pi^0$ 's produced in the MicroBooNE TPC are produced through  
 886 neutron inelastic scattering.

887 In total, 90,297 CORSIKA truth events were produced to constrain production rates for  
 888 signal and background. From that, a random sample of 10K events were ran through the  
 889 wire-cell imaging reconstruction. Additionally, a signal sample of events contains a single  
 890 neutron  $\pi^0$  of  $\approx 1.2K$  was produced and reconstructed through the wire-cell imaging. The  
 891 exact rates will be discussed in Chapter 7.

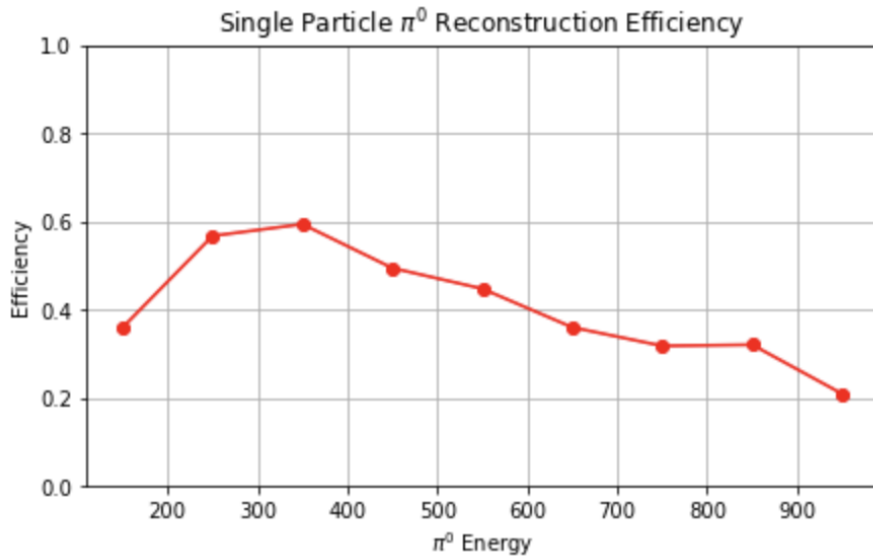


Figure 6.8: The plot shows the  $\pi^0$  reconstruction efficiency for  $\pi^0$ 's over a 1000-10,000 MeV energy range. The reconstruction efficiency peaks around 350 MeV which conveniently is around the production energy for cosmic  $\pi^0$

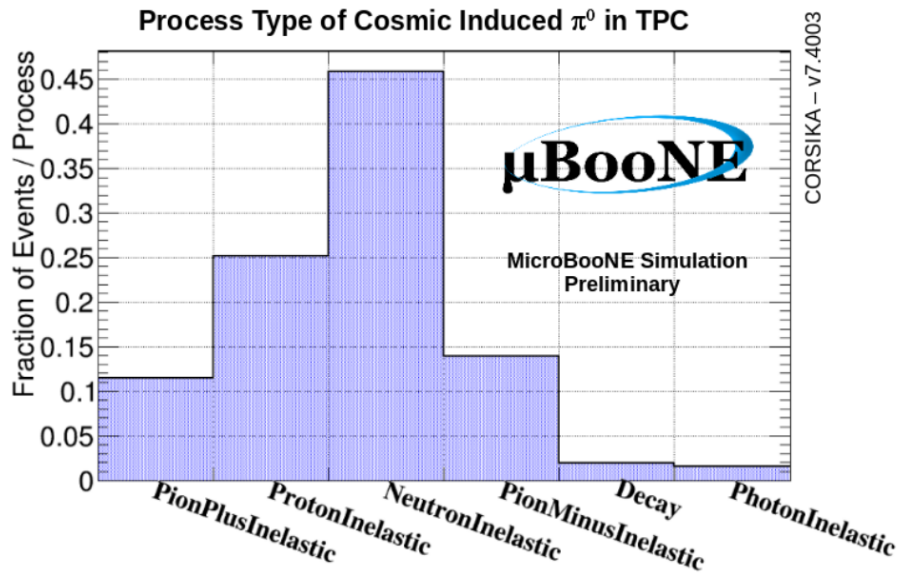


Figure 6.9: Physical process for cosmic  $\pi^0$  that decay inside the TPC.

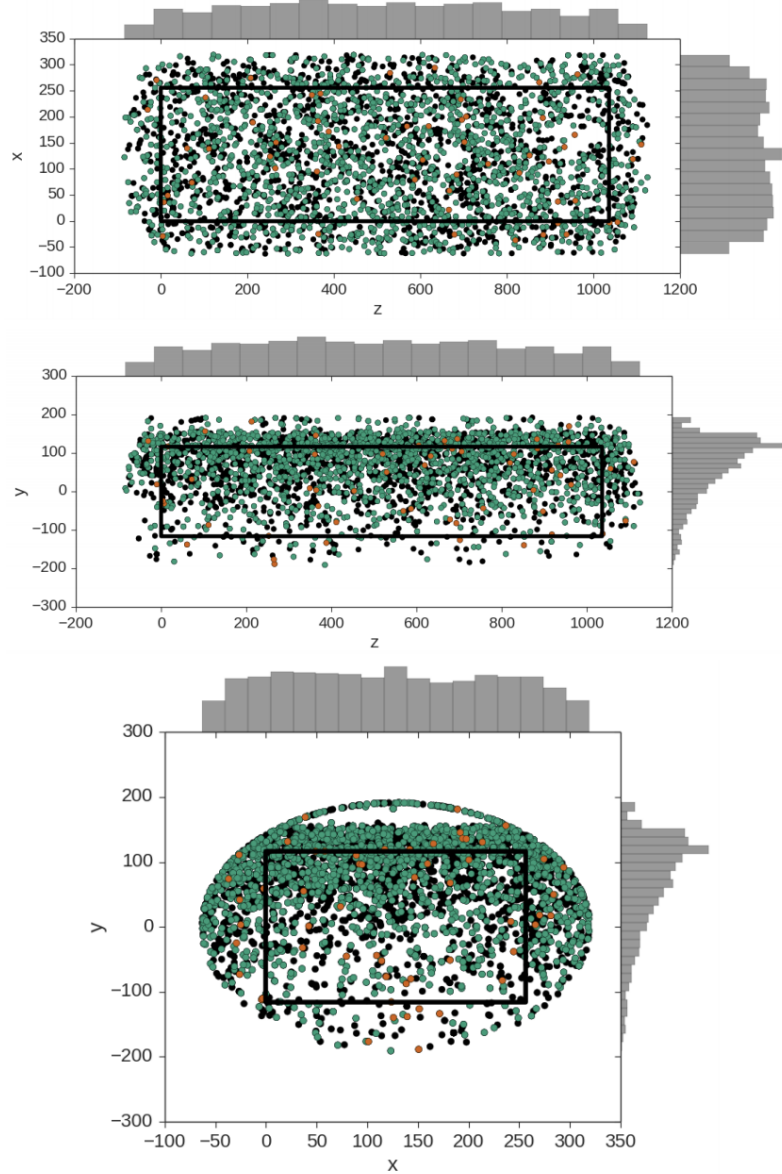


Figure 6.10: These plots show the decay point of actual cosmic  $\pi^0$ 's throughout any time in the 4.8 ms window. The green points represent neutron induced  $\pi^0$ 's, the orange represent photon induced  $\pi^0$ 's, and the black represent a  $\pi^0$  that was produced from a charged particle. In each plot the black box is to represent the entire TPC dimensions not including fiducial cuts. Note that this is a stacked scatter plot with ordering; charged particle(black), photon(orange), neutron(green).

## 892 Chapter 7

# 893 Results

894 The goal of this study primarily two fold. The first goal is to highlight a different technique  
895 to reconstruct  $\pi^0$  and EM-showers in an LArTPC. To best showcase this reconstruction  
896 technique we will focus on reconstructing  $\pi^0$ 's that are induced from a single neutron. In  
897 many instances, neutral induced interactions do not have a vertex. Reconstructing EM  
898 showers from a  $\pi^0$  decay without a vertex poses many challenges for traditional techniques.  
899 The Wire-Cell imaging approach allows for a full 3D shower reconstruction without the use  
900 of a vertex. The second goal is to measure and compare the cosmic ray neutron induced  
901  $1-\pi^0$  production rate in the MicroBooNE detector. This reconstruction technique is well  
902 suited for this type of analysis.

903 This section will address results from both Monte Carlo and actual MicroBooNE cosmics  
904 data. To be clear, we will define our signal to be events that produce 1 and only 1 neutron  
905 induce single  $\pi^0$  inside the TPC fiducial volume. For this analysis the fiducial volume is  
906 defined from: X [0,256] , Y[-116,116], Z[400,800]. We also restrict our bounds to events that  
907 happen in 1 drift window as defined in section ??

### 908 7.1 Monte Carlo Simulation

909 First, a word on simulation constraints. While the wire-cell imaging process provides consid-  
910 erable gains towards extracting high resolution LArTPC reconstruction, it does come with  
911 a high computational cost. This was an issue for generating a large sample of Monte Carlo

Table 7.1: Cosiska MC rates

Neutron induced 1 $\pi^0$	1,255
Neutron induced 1 $\pi^0$ outside	13,434
Proton induced 1 $\pi^0$ outsize	5,038
Other induced 1 $\pi^0$	9,530
no 1 $\pi^0$ or multi $\pi^0$	61,040

for Wire-Cell imaging. The process should be able to be distributed, but for this analysis it this process was not yet available. This required us to use an upsampling technique with the background Monte Carlo sample which is describe in the subsequent paragraphs.

First a enhanced sample of 1,255 signal events were generated from CORSIKA, processed through wire-cell imaging, and reconstructed with the described process in section 6. A background only sample, consisting of 8,720 randomly sampled background events were processed through processed through wire-cell imaging and the reconstruction. This number was then scaled by 0.0139 to obtain an absolute background value relative to the enhanced signal sample. This scaling represents a new total of 90,297 events. One event corresponds to 1 MicroBooNE readout frame.

From the total sample we find that 1.39% are signal. The remaining background is divided into 5 categories: 1. proton induced events that produce 1  $\pi^0$  either inside or outside the fiducial volume, 2. neutron induced events that are produced outside the fiducial volume , 3. Events that produce 1  $\pi^0$  either inside or outside the fiducial volume not coming from a proton or neutron, 4. Multi  $\pi^0$  produced either inside or outside the fiducial volume, 4. Events that do not contain any  $\pi^0$  . Table 7.1 shows the corresponding counts from the 90,297 CORSIKA sample.

Next, the selection cuts described in chapter 6 are applied to both the signal sample. There are a total of 443 events that pass the cuts made in section 6. This corresponds to a signal efficiency of 35.9%. A plot for the reconstructed mass is shown in figure 7.1. The mass peak, which is supposed to be around  $135 \text{ MeV}/c^2$ , is centered around  $100 \text{ MeV}/c^2$  due to the missing energy. This is in agreement with what we expect from the single particle  $\pi^0$  studies from section 6.

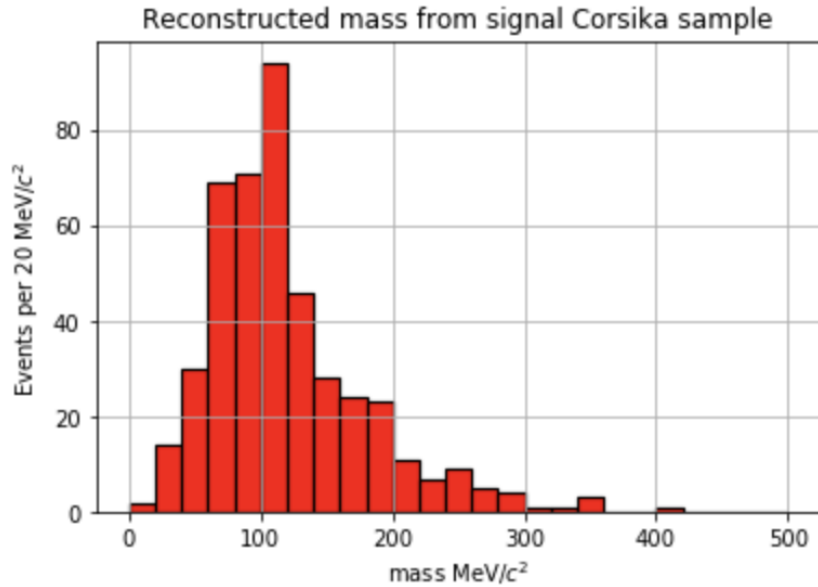


Figure 7.1: Plot of the mass distribution for neutron induced signal signal events.

935 Then, the same cuts were applied to the background only sample. We find there to be  
 936 a background rate of 2.3%. Ultimately resulting in a signal:background of 0.21 ( Approximately  
 937 1 : 5.6 ). A plot of the reconstructed mass distribution for the entire background is  
 938 shown in figure 7.2

939 It is important to note that the background distribution will also contain  $\pi^0$  events. The  
 940 background distribution as described in section 7.1 is plotted in figure ?? The distribution  
 941 should also have some well reconstructed  $\pi^0$ . For this analysis, since we did not require the  
 942 use of a vertex there is a sizable portion of background that are actual reconstructed  $\pi^0$ . This  
 943 comes from two primary effects both of which are products of how the reconstruction criteria  
 944 is defined. The first effect is part of the group coming from events with No  $\pi^0$  group. Many  
 945 of the events are actual  $\pi^0$  particles but reconstructed out side of the fiducial volume.  
 946 The second effect is in the remaining  $\pi^0$  groups which obviously contains at least one  
 947  $\pi^0$ . Being that we remove as many track as possible, Many proton and charged pion tracks  
 948 are removed. The in eyes of the selection process a proton or charged pion induced  $\pi^0$  event  
 949 has a near identical topology to the signal.

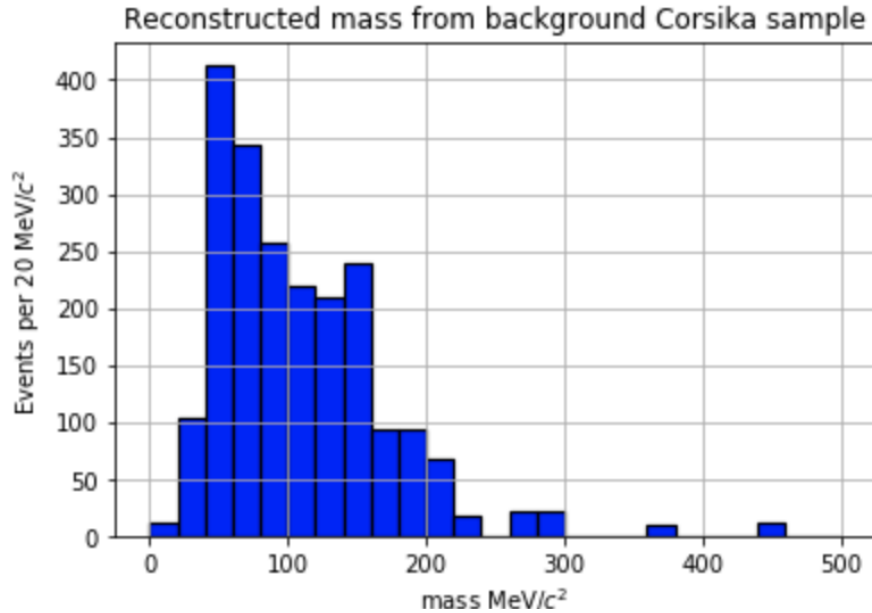


Figure 7.2: Plot of the mass distribution for cosmic background events.

## 950 7.2 Data

951 The same selection cuts were applied to a dataset of 13,022 off beam cosmic data events  
 952 that were sampled from the 'MicroBooNE Good Run List'. This is an internal list that  
 953 MicroBoone generates to define when the detector is in acceptable running mode. This list  
 954 takes into account various aspects of the detector such as; wire stability, argon purity, PMT  
 955 response, etc. It is important to note that the data sample that is used in this thesis is only  
 956 from the good run list. Doing this, assumes that any bias in the sample is averaged over  
 957 for interaction type. The mass distribution is calculated from the given 13,022 sample and  
 958 there is a clear mass peak from the  $\pi^0$ 's that is also centered below the actual  $135 \text{ MeV}/c^2$   
 959 mass.

## 960 7.3 Data-Monte Carlo Comparison

961 To better understand the data distribution, we first plot an area normalized histogram for  
 962 Monte Carlo and Data. This is shown in figure 7.3. We see that the shape is indeed similar  
 963 but not ideal. The lack of smoothness in the Monte Carlo is due to the upsampling. Given

964 this, the area normalized shape comparison only serves the purpose of showing that we  
 965 believe we are reconstructing  $\pi^0$ 's and reasonably handling the background.

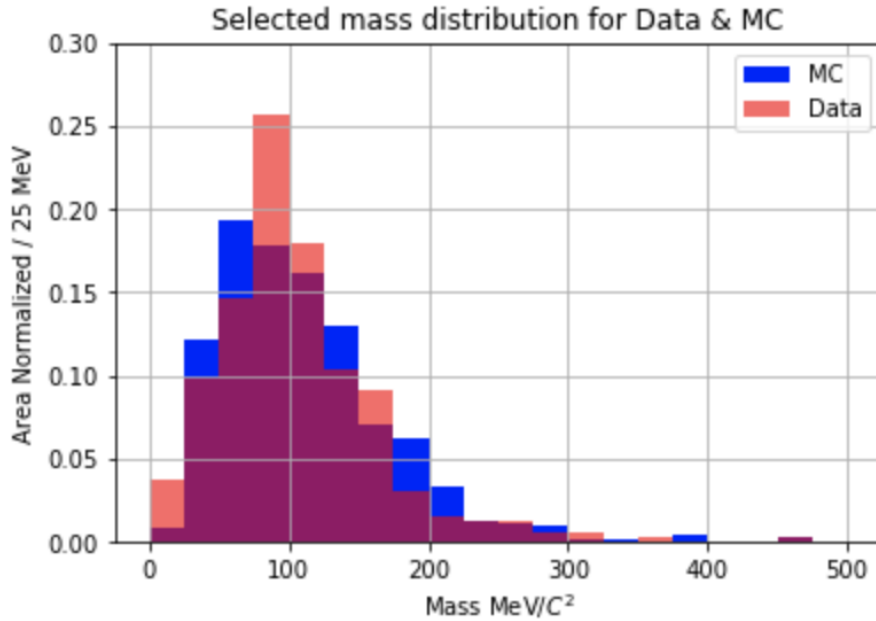


Figure 7.3: Area normalized Data-Monte Carlo mass distributions. The shapes between the data and Monte Carlo distributions provide confidence that we are reconstructing  $\pi^0$ 's in the distribution.

966 To better compare data and Monte Carlo an absolute rate comparison should be made.  
 967 This will address how well the Monte Carlo represents the data. The mass distribution is  
 968 shown in Figure 7.4. Out of the box, Corsika slightly over predicts the rate from data. To  
 969 address this, a  $\chi^2$  minimization can be performed fit the Monte Carlo to the data. Both the  
 970 signal and background are varied to optimize the fit to data. We find that the fit returns  
 971 a minimum of  $20.3 \chi^2/df$  when the signal is reduced by 72% and the background is also  
 972 reduced by 84%. The adjusted mass distribution from the fit is shown in Figure 7.5

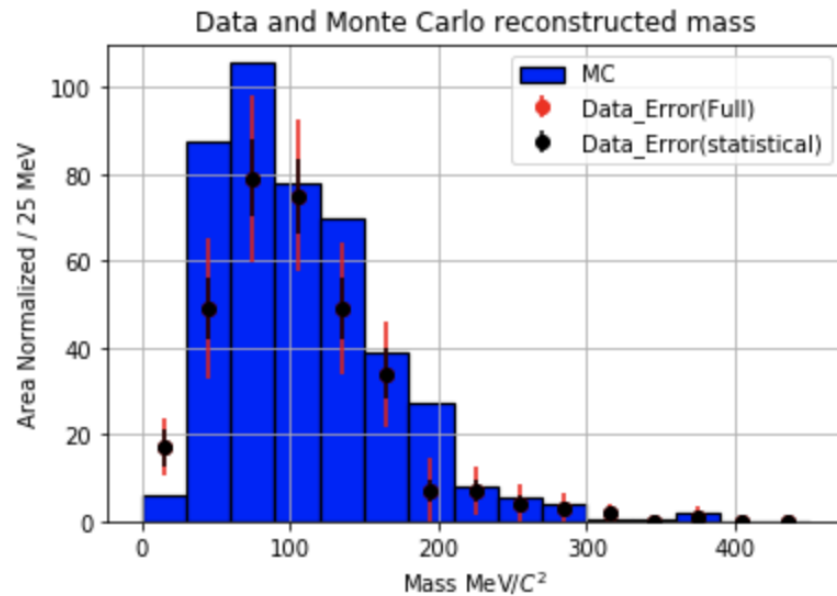


Figure 7.4: This plot shows the mass distribution from data with respect to the unchanged Monte Carlo.

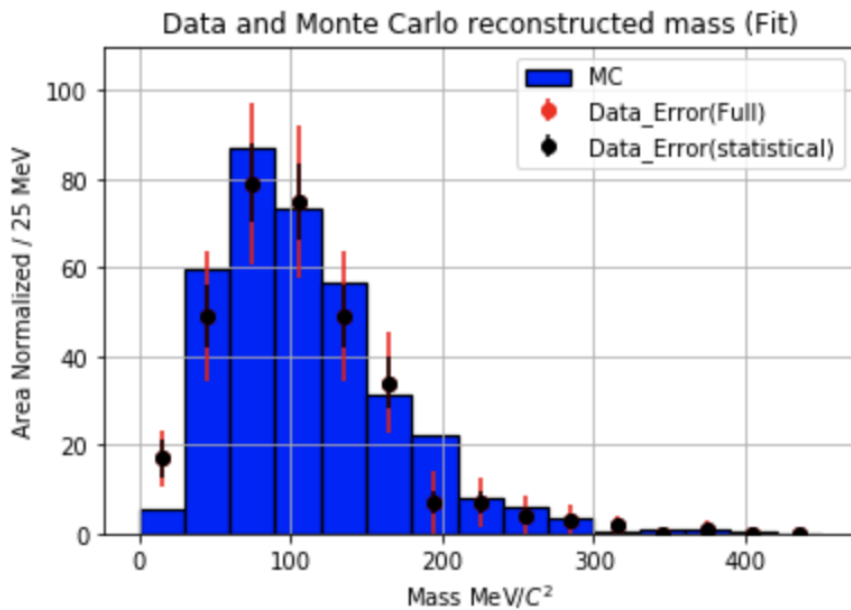


Figure 7.5: This plot shows the mass distribution from data with respect to the fitted Monte Carlo.

# 973 Chapter 8

## 974 Conclusions

### 975 8.1 Conclusion

976 The construction of MicroBooNE is an essential step forward for the low energy neutrino  
977 physics community. The R&D process provided valuable insights towards future LArTPC  
978 detector technology. The MicroBooNE detector was completed in 2015 and has since been  
979 collecting valuable data.

980 This thesis showcases a radically new technique for 3D reconstruction of EM showers.  
981 Although wire-cell does require a high amount of computational resources, the improved  
982 3D reconstruction capabilities for EM showers provide justification. Additionally, we are  
983 able to reconstruct  $\pi^0$ 's without the use of vertex information. We have built an algorithm  
984 to identify neutron induced single  $\pi^0$  events. We found that the current CORSIKA Monte  
985 Carlo slightly over predicts the rate of neutron induced  $\pi^0$  in the MicroBooNE detector. The  
986 data used in this thesis is entirely on cosmic ray data but the extension to neutral current  
987 single  $\pi^0$  interaction is the next logical step.

<sup>988</sup> **Bibliography**

## Part I

989

## Appendices

990

<sup>991</sup> **Bibliography**